Furthermore, an α4β2 nAChR antagonist, dihydro-β-erythroidine (DHβE) completely blocked the neuroprotective effect of 5IA (Glu alone: 44±9%, 5IA: 67±6%, 5IA+DHβE: 49±8%) (Fig. 6A), while an α7 nAChR antagonist, α-bungarotoxin (α-BGT) had no effect on 5IA-induced neuroprotection (Glu alone: 48± 9%, 5IA: 68±5%, 5IA+α-BGT: 64±6%) (Fig. 6B).

2.3. Effects of extracellular calcium ion on 5IA-induced neuroprotection

Finally, we studied the effects of extracellular Ca^{2+} on the protective effect of 5IA against Glu-induced neurotoxicity. Cultures were preincubated with or without 5IA in EMEM (including Ca^{2+}) or S-MEM (Ca^{2+}-free EMEM) for 2 h, and then 10-min Glu exposure and 2-h drug-free incubation were performed in EMEM. As shown in Fig. 7, although the pretreatment of 5IA in Ca^{2+}-including medium attenuated Glu-induced neurotoxicity, pretreatment in Ca^{2+}-free medium could not block toxicity (Glu alone: 49±4%, 5IA with Ca^{2+}: 72±7%, 5IA without Ca^{2+}: 51±4%). The cultures incubated in Ca^{2+}-free medium maintained high viability under Glu-free conditions (91±4%) (Fig. 7).

3. Discussion

In the present study, we investigated the effects of 5IA on Glu-induced neurotoxicity using primary cultures of rat cortical neurons. 5IA prevented Glu-induced neurotoxicity both in a time- and concentration-dependent manner. 5IA-induced neuroprotection required pretreatment of 5IA prior to Glu exposure. Treatment after Glu exposure could not rescue the cultured cells. These results are consistent with previous reports that investigated the neuroprotective effects of other nAChR agonists against Glu-mediated toxicity (Akaike et al., 1994; Donnelly-Roberts et al., 1996; Shimohama et al., 1996), although the concentration of nAChR agonists used was quite different. In our study, 10 nM of 5IA showed comparable neuroprotective effects to previous reports in which 10 μM of nicotine or ABT-418 was used. Moreover, in an FLIPR assay using HEK-293 cells stably expressing human α4β2 nAChRs, 5IA showed about 50 times higher EC_{50} values than TC-2559 (Zwart et al., 2006), which showed similar efficacy and potency to nicotine and ABT-418 on Rb^+ release from rat thalamic synaptosomes (Bencherif et al., 2000). These results indicate that 5IA has much higher efficacy and potency on α4β2 nAChRs than other nAChR agonists.

Next, we examined which subtype of acetylcholine receptor was involved in the neuroprotective effect of 5IA using nicotinic and muscarinic antagonists. As expected, mecamylamine antagonized the effect of 5IA completely but scopolamine did not. Moreover, DHβE also blocked 5IA-induced neuroprotection completely, while α-BGT had no effect. This result suggests that the neuroprotective effect of 5IA is mediated only by α4β2 nAChRs and that neither α7 nAChRs nor muscarinic acetylcholine receptors are involved in the effect of 5IA. This result is in contrast to many studies that have reported neuroprotection evoked by nAChR stimulation against Glu-induced cytotoxicity mediated, at least in part, by α7 nAChRs (Akaike et al., 1994; Donnelly-Roberts et al., 1996; Kaneko et al., 1997; Takada et al., 2003). Muhkin et al. reported that the α7/α4β2 ratio calculated from the

Ki value of 5IA was 25,000, whereas that of nicotine was only 170 (Mukhin et al., 2000); that is to say, 5IA had approximately 150 times greater selectivity for α4β2 nAChRs than nicotine. Because of this selectivity, it is likely that 5IA, at the low concentration used in this study, acted almost entirely on α4β2 nAChRs. This suggests that 5IA could be useful to elucidate the mechanism of α4β2 nAChR-mediated neuroprotection.

Although excessive influx of Ca^{2+} causes neuronal death, increases of intracellular Ca^{2+} can trigger the activation of Ca^{2+}-dependent protein kinases involved in neuroprotective cell signaling. α4β2 nAChRs are reported to be to Ca^{2+}-permeable although less so than α7 nAChRs (Jensen et al., 2005). Moreover, they are permeable to monovalent cations and the influx of Na^+ could depolarize the cell thereby activating voltage-gated Ca^{2+} channels (VGCCs) and increase Ca^{2+} entry (Nakayama et al., 2001). Consequently, we investigated the effect of extracellular Ca^{2+} on 5IA-mediated neuroprotective action. As shown in Fig. 7, the protective effect of 5IA was diminished by removing extracellular Ca^{2+}. This result demonstrates that extracellular Ca^{2+} plays a critical role in neuroprotection mediated not only by α7 nAChRs (Donnelly-Roberts et al., 1996) but also by α4β2 nAChRs. In fact, Dickinson et al. have recently demonstrated that the primary route of Ca^{2+} entry following 5IA treatment is via L-type VGCC and that the resulting increases of intracellular Ca^{2+} were α-BGT-insensitive (Dickinson et al., 2007). Thus, the influx of Ca^{2+} through α4β2 nAChRs and/or through VGCCs induced by the activation of α4β2 nAChRs could play a role in the neuroprotective action of 5IA.

Further mechanisms underlying 5IA-induced neuroprotection have not yet been elucidated. The activation of Ca^{2+}/calmodulin-dependent protein kinase II (CaMKII), phosphatidylinositol 3-kinase (PI3-K) and the downstream PI3-K target Akt have been reported to be important in the calcium-mediated promotion of survival in neurons (Ikegami and Koike, 2000). Vaillant et al. reported that Ca^{2+} influx via VGCCs was involved in activation of the CaMKII pathway and Ras–PI3-K–Akt pathway (Vaillant et al., 1999); therefore, 5IA-induced neuroprotection potentially occurs through both of these pathways.

Neurotrophic factors may also be involved in 5IA-induced neuroprotection. It was reported that ABT-594, an analogue of 5IA, increased fibroblast growth factor-2 (FGF-2) mRNA levels (Belluardo et al., 1999) and that FGF-2 protected cultured neurons from NMDA-mediated excitotoxicity (Freese et al., 1992). Moreover, Roceri et al. reported that the expression of FGF-2 was regulated in a Ca^{2+}-dependent manner (Roceri et al., 2000). Thus, it is possible that 5IA shows neuroprotective effects by affecting the expression of FGF-2.

In summary, we have revealed that 5IA has neuroprotective effects against Glu-induced cytotoxicity at a much lower concentration than other nAChR agonists. These effects required the treatment of 5IA prior to Glu exposure and were mediated not by α7 nAChRs but by α4β2 nAChRs. Moreover, extracellular Ca^{2+} was essential for 5IA-induced neuroprotection. These findings suggest that the neuroprotective effects of 5IA are produced by the activation of α4β2 nAChRs followed by the influx of extracellular Ca^{2+}. In conclusion, 5IA is possibly more useful for the treatment and prevention of neurodegenerative diseases than other nAChR agonists because of its high efficacy and selectivity, and should be a valuable tool for elucidating the mechanism of neuroprotection associated with α4β2 nAChRs.

4. Experimental procedures

4.1. Materials

Eagle's minimal essential salt medium (EMEM) was purchased from Nissui Pharmaceutical (Tokyo, Japan). Ca^{2+}-free EMEM (S-MEM) was purchased from Invitrogen (Carlsbad, CA). Fetal bovine serum and horse serum were purchased from JRH Biosciences (Lenexa, KS) and Invitrogen, respectively. Drugs were obtained from the following sources: D-(+)-glucose, sodium hydrogen carbonate ($NaHCO_3$), HEPES, L-glutamic acid monosodium salt and trypan blue (Nacalai Tesque, Kyoto, Japan), cytosine-1-β-D(+)-arabinofuranoside (Ara-C) (Wako Pure Chemical Industries, Osaka, Japan), L-glutamine, mecamylamine hydrochloride and dihydro-β-erythroidine hydrobromide (Sigma-Aldrich, St. Louis, MO), (−)-scopolamine hydrobromide (RBI, Natick, MA), α-bungarotoxin and ionomycin (EMD Biosciences, San Diego, CA). 5IA was synthesized according to the previously published methods (Saji et al., 2002).

4.2. Cell culture

Animals were treated in accordance with the guidelines of the Kyoto University Animal Care Committee.

Primary cultures were obtained from the cerebral cortex of fetal rats (17–18 days of gestation) using a modified method described previously (Takada-Takatori et al., 2006) with a slight modification. Briefly, single cells dissociated from the whole cerebral cortex of fetal rats were plated on plastic coverslips attached in 60 mm dishes (4.5×10^6 cells per dish). Cultures were incubated in EMEM supplemented with 5% heat-inactivated fetal bovine serum and 5% heat-inactivated horse serum (1–7 days after plating) or 5% heat-inactivated horse serum (8–12 days after plating), L-glutamine (2 mM), D-(+)-glucose (11 mM), $NaHCO_3$ (24 mM) and HEPES (10 mM). Cultures were maintained at 37 °C in a humidified 5% CO_2 atmosphere. After 6 days of plating, non-neuronal cells were removed by the addition of Ara-C (10 μM). Only mature cultures (11–12 days in vitro) were used for experiments.

4.3. Drug treatment

Exposure to Glu (1 mM) was carried out in EMEM. The cultures were exposed to Glu for 10 min and then incubated in drug-free EMEM for 2 h. Unless otherwise indicated, 5IA was applied for 2 h before and 10 min during Glu exposure. Cholinergic antagonists (MEC, SCOP, DHβE and α-BGT) were added to EMEM concomitant with 5IA. All experiments were performed at 37 °C.

4.4. Measurement of neurotoxicity

Neurotoxicity induced by Glu was quantitatively assessed by examining cultures under Hoffman modulation microscopy as described previously (Kitamura et al., 2006; Taguchi et al., 2003) with a slight modification. Cell viability was assessed by the trypan blue exclusion method, i.e., cell cultures were stained with 1.5% trypan blue solution for 3 min at room temperature and then rinsed with physiological saline. The stained cells were regarded as non-viable. In each experiment, cells on five coverslips were counted to obtain the means±s.d. of cell viability.

4.5. Statistics

Data are expressed as the means±s.d. The statistical significance of difference between groups was determined by one-way analysis of variance (ANOVA) followed by Tukey–Kramer multiple comparison tests. Differences were considered significant when $p < 0.05$.

REFERENCES

Akaike, A., Tamura, Y., Yokota, T., Shimohama, S., Kimura, J., 1994. Nicotine-induced protection of cultured cortical neurons against N-methyl-D-aspartate receptor-mediated glutamate cytotoxicity. Brain Res. 644, 181–187.

Arias, C., Becerra-Garcia, F., Tapia, R., 1998. Glutamic acid and Alzheimer's disease. Neurobiology. (Bp). 6, 33–43.

Belluardo, N., Mudo, G., Caniglia, G., Cheng, Q., Blum, M., Fuxe, K., 1999. The nicotinic acetylcholine receptor agonist ABT-594 increases FGF-2 expression in various rat brain regions. Neuroreport 10, 3909–3913.

Belluardo, N., Mudo, G., Blum, M., Fuxe, K., 2000. Central nicotinic receptors, neurotrophic factors and neuroprotection. Behav. Brain Res. 113, 21–34.

Bencherif, M., Bane, A.J., Miller, C.H., Dull, G.M., Gatto, G.J., 2000. TC-2559: a novel orally active ligand selective at neuronal acetylcholine receptors. Eur. J. Pharmacol. 409, 45–55.

Burghaus, L., Schutz, U., Krempel, U., de Vos, R.A., Jansen Steur, E.N., Wevers, A., Lindstrom, J., Schroder, H., 2000. Quantitative assessment of nicotinic acetylcholine receptor proteins in the cerebral cortex of Alzheimer patients. Brain Res. Mol. Brain Res. 76, 385–388.

Burghaus, L., Schutz, U., Krempel, U., Lindstrom, J., Schroder, H., 2003. Loss of nicotinic acetylcholine receptor subunits alpha4 and alpha7 in the cerebral cortex of Parkinson patients. Parkinsonism Relat. Disord. 9, 243–246.

Dickinson, J.A., Hanrott, K.E., Mok, M.H., Kew, J.N., Wonnacott, S., 2007. Differential coupling of alpha7 and non-alpha7 nicotinic acetylcholine receptors to calcium-induced calcium release and voltage-operated calcium channels in PC12 cells. J. Neurochem. 100, 1089–1096.

Donnelly-Roberts, D.L., Xue, I.C., Arneric, S.P., Sullivan, J.P., 1996. In vitro neuroprotective properties of the novel cholinergic channel activator (ChCA), ABT-418. Brain Res. 719, 36–44.

Freese, A., Finklestein, S.P., DiFiglia, M., 1992. Basic fibroblast growth factor protects striatal neurons in vitro from NMDA-receptor mediated excitotoxicity. Brain Res. 575, 351–355.

Fujita, M., Ichise, M., Zoghbi, S.S., Liow, J.S., Ghose, S., Vines, D.C., Sangare, J., Lu, J.Q., Cropley, V.L., Iida, H., Kim, K.M., Cohen, R.M., Bara-Jimenez, W., Ravina, B., Innis, R.B., 2006. Widespread decrease of nicotinic acetylcholine receptors in Parkinson's disease. Ann. Neurol. 59, 174–177.

Gotti, C., Fornasari, D., Clementi, F., 1997. Human neuronal nicotinic receptors. Prog. Neurobiol. 53, 199–237.

Ikegami, K., Koike, T., 2000. Membrane depolarization-mediated survival of sympathetic neurons occurs through both phosphatidylinositol 3-kinase- and CaM kinase II-dependent pathways. Brain Res. 866, 218–226.

Jensen, A.A., Frolund, B., Liljefors, T., Krogsgaard-Larsen, P., 2005. Neuronal nicotinic acetylcholine receptors: structural revelations, target identifications, and therapeutic inspirations. J. Med. Chem. 48, 4705–4745.

Kaneko, S., Maeda, T., Kume, T., Kochiyama, H., Akaike, A., Shimohama, S., Kimura, J., 1997. Nicotine protects cultured cortical neurons against glutamate-induced cytotoxicity via alpha7-neuronal receptors and neuronal CNS receptors. Brain Res. 765, 135–140.

Kihara, T., Sawada, H., Nakamizo, T., Kanki, R., Yamashita, H., Maelicke, A., Shimohama, S., 2004. Galantamine modulates nicotinic receptor and blocks Abeta-enhanced glutamate toxicity. Biochem. Biophys. Res. Commun. 325, 976–982.

Kitamura, Y., Iida, Y., Abe, J., Ueda, M., Mifune, M., Kasuya, F., Ohta, M., Igarashi, K., Saito, Y., Saji, H., 2006. Protective effect of zinc against ischemic neuronal injury in a middle cerebral artery occlusion model. J. Pharmacol. Sci. 100, 142–148.

Meldrum, B., Garthwaite, J., 1990. Excitatory amino acid neurotoxicity and neurodegenerative disease. Trends Pharmacol. Sci. 11, 379–387.

Mukhin, A.G., Gundisch, D., Horti, A.G., Koren, A.O., Tamagnan, G., Kimes, A.S., Chambers, J., Vaupel, D.B., King, S.L., Picciotto, M.R., Innis, R.B., London, E.D., 2000. 5-Iodo-A-85380, an alpha4beta2 subtype-selective ligand for nicotinic acetylcholine receptors. Mol. Pharmacol. 57, 642–669.

Nakayama, H., Numakawa, T., Ikeuchi, T., Hatanaka, H., 2001. Nicotine-induced phosphorylation of extracellular signal-regulated protein kinase and CREB in PC12h cells. J. Neurochem. 79, 489–498.

O'Brien, J.T., Colloby, S.J., Pakrasi, S., Perry, E.K., Pimlott, S.L., Wyper, D.J., McKeith, I.G., Williams, E.D., 2007. Alpha4beta2 nicotinic receptor status in Alzheimer's disease using 123I-5IA-85380 single-photon-emission computed tomography. J. Neurol. Neurosurg. Psychiatry 78, 356–362.

Oishi, N., Hashikawa, K., Yoshida, H., Ishizu, K., Ueda, M., Kawashima, H., Saji, H., Fukuyama, H., 2007. Quantification of nicotinic acetylcholine receptors in Parkinson's disease with (123)I-5IA SPECT. J. Neurol. Sci. 256, 52–60.

Paterson, D., Nordberg, A., 2000. Neuronal nicotinic receptors in the human brain. Prog. Neurobiol. 61, 75–111.

Roceri, M., Molteni, R., Racagni, G., Riva, M.A., 2000. Calcium-dependent modulation of FGF-2 expression in cultured cerebellar granule neurons. Neuroreport 11, 3615–3619.

Saji, H., Ogawa, M., Ueda, M., Iida, Y., Magata, Y., Tominaga, A., Kawashima, H., Kitamura, Y., Nakagawa, M., Kiyono, Y., Mukai, T., 2002. Evaluation of radioiodinated 5-iodo-3-(2(S)-azetidinylmethoxy)pyridine as a ligand for SPECT investigations of brain nicotinic acetylcholine receptors. Ann. Nucl. Med. 16, 189–200.

Shimohama, S., Kihara, T., 2001. Nicotinic receptor-mediated protection against beta-amyloid neurotoxicity. Biol. Psychiatry 49, 233–239.

Shimohama, S., Taniguchi, T., Fujiwara, M., Kameyama, M., 1986. Changes in nicotinic and muscarinic cholinergic receptors in Alzheimer-type dementia. J. Neurochem. 46, 288–293.

Shimohama, S., Akaike, A., Kimura, J., 1996. Nicotine-induced protection against glutamate cytotoxicity. Nicotinic cholinergic receptor-mediated inhibition of nitric oxide formation. Ann. N.Y. Acad. Sci. 356–361.

Taguchi, R., Nishikawa, H., Kume, T., Terauchi, T., Kaneko, S., Katsuki, H., Yonaga, M., Sugimoto, H., Akaike, A., 2003. Serofendic acid prevents acute glutamate neurotoxicity in cultured cortical neurons. Eur. J. Pharmacol. 477, 195–203.

Takada, Y., Yonezawa, A., Kume, T., Katsuki, H., Kaneko, S., Sugimoto, H., Akaike, A., 2003. Nicotinic acetylcholine receptor-mediated neuroprotection by donepezil against glutamate neurotoxicity in rat cortical neurons. J. Pharmacol. Exp. Ther. 306, 772–777.

Takada-Takatori, Y., Kume, T., Sugimoto, M., Katsuki, H., Sugimoto, H., Akaike, A., 2006. Acetylcholinesterase inhibitors used in treatment of Alzheimer's disease prevent glutamate neurotoxicity via nicotinic acetylcholine receptors and phosphatidylinositol 3-kinase cascade. Neuropharmacology 51, 474–486.

Ueda, M., Iida, Y., Mukai, T., Mamede, M., Ishizu, K., Ogawa, M., Magata, Y., Konishi, J., Saji, H., 2004. 5-[123I]Iodo-A-85380: assessment of pharmacological safety, radiation dosimetry and SPECT imaging of brain nicotinic receptors in healthy human subjects. Ann. Nucl. Med. 18, 337–344.

Vaillant, A.R., Mazzoni, I., Tudan, C., Boudreau, M., Kaplan, D.R., Miller, F.D., 1999. Depolarization and neurotrophins converge on the phosphatidylinositol 3-kinase-Akt pathway to synergistically regulate neuronal survival. J. Cell Biol. 146, 955–966.

Vaupel, D.B., Tella, S.R., Huso, D.L., Mukhin, A.G., Baum, I., Wagner, V.O., Horti, A.G., London, E.D., Koren, A.O., Kimes, A.S., 2003. Pharmacology, toxicology, and radiation dosimetry evaluation of [I-123]5-I-a-85380, a radioligand for in vivo imaging of cerebral neuronal nicotinic acetylcholine receptors in humans. Drug Dev. Res. 58, 149–168.

Zwart, R., Broad, L.M., Xi, Q., Lee, M., Moroni, M., Bermudez, I., Sher, E., 2006. 5-I A-85380 and TC-2559 differentially activate heterologously expressed alpha4beta2 nicotinic receptors. Eur. J. Pharmacol. 539, 10–17.

Temporal Change in Human Nicotinic Acetylcholine Receptor After Smoking Cessation: 5IA SPECT Study

Marcelo Mamede[1], Koichi Ishizu[1], Masashi Ueda[2], Takahiro Mukai[1], Yasuhiko Iida[2], Hidekazu Kawashima[2], Hidenao Fukuyama[3], Kaori Togashi[1], and Hideo Saji[2]

[1]Department of Diagnostic Imaging and Nuclear Medicine, Graduate School of Medicine, Kyoto University, Kyoto, Japan; [2]Department of Patho-Functional Bioanalysis, Graduate School of Pharmaceutical Science, Kyoto University, Kyoto, Japan; and [3]Brain Function Imaging Division, Human Brain Research Center, Graduate School of Medicine, Kyoto University, Kyoto, Japan

Nicotinic acetylcholine receptors (nAChRs) are of great interest because they are implicated in various brain functions. They also are thought to play an important role in nicotine addiction of smokers. Chronic (−)-nicotine, a nAChR agonist, treatment in mice and rats elicits a dose-dependent increase in nAChRs in the brain. Upregulation of nAChRs in postmortem human brains of smokers has also been reported. However, changes in nAChRs after cigarette smoking cessation in humans are poorly understood. The aim of this study was to detect the dynamic changes of nAChRs after smoking and smoking cessation in the brains of living subjects. **Methods:** We performed 5-^{123}I-iodo-A-85380 ([123]I-5IA) SPECT on nonsmokers and smokers (n = 16) who had quit smoking for 4 h, 10 d, and 21 d and calculated and compared distribution volumes (Vt) of [123]I-5IA. **Results:** The binding potential of nAChRs (Vt of [123]I-5IA) in the brains of smokers decreased by 33.5% ± 10.5% after 4 h of smoking cessation, increased by 25.7% ± 9.2% after 10 d of smoking cessation, and decreased to the level of nonsmokers after 21 d of smoking cessation. **Conclusion:** Because the upregulation of the nAChRs of the smokers after chronic exposure of the nicotine was downregulated to the nonsmokers' level by around 21 d after smoking cessation, the upregulation is a temporary effect. The decrease in nicotinic receptors to nonsmoker levels may be the breaking point during the nicotine withdrawal period.

Key Words: [123]I-5IA; SPECT; nicotinic acetylcholine receptors; human brain; smoking withdrawal; quantitative measurement

Nicotinic acetylcholine receptors (nAChRs) are a family of ligand-gated ion channels that regulate neurotransmission in the central and peripheral nervous systems. These receptors are of great interest because they are implicated in various brain functions, including cognition and memory (*1,2*) and in nicotine-induced neuroprotective (*3*) and analgesic effects (*4*). In addition, these receptors are thought to play an important role in nicotine addiction (*5*).

Chronic treatment with agonists for most neurotransmitter receptor systems results in a decrease in receptor number. However, it has been demonstrated that chronic treatment of mice (*6*) and rats (*7*) with (−)-nicotine, an nAChR agonist, elicits a dose-dependent increase in nAChRs. This upregulation is not permanent, returning to control levels within 7–10 d in mice (*6*) and 15–20 d in rats (*8,9*) after cessation of (−)-nicotine treatment. Previous efforts to demonstrate nAChR upregulation in the human brain have also been reported primarily in in vitro binding assays (*10,11*). Kassiou et al. reported the upregulation of nAChRs with chronic (−)-nicotine treatment in the brain of a live baboon (*12*). More recently, Staley et al. described the upregulation of nAChRs in human brains after early abstinence of tobacco smoking using 5-^{123}I-iodo-A-85380 ([123]I-5IA) and SPECT images (*13*). However, changes in nAChRs in humans after cessation of smoking are poorly understood. Breese et al. studied the levels of ^{3}H-nicotine binding in humans postmortem for changes in nicotinic receptor levels and reported that the nAChR levels in smokers who had stopped smoking at least 2 mo before their death were similar to those in nonsmokers (*14*); the effects of shorter-term smoking cessation are unknown.

[123]I-5IA is a nAChR imaging probe that has extremely high selectivity and specificity for the α4β2 subunit of nAChRs in rodent (inhibition constant = 0.37 nM) (*15*) and primate brain in vivo (*16*), with relatively low acute toxicity (effective dose equivalent = 30 μSv/MBq) (*17,18*). Moreover, we have developed the methodology for the quantification of nAChRs in human brain using [123]I-5IA and SPECT (*19*).

The aim of the present study was to detect the dynamic changes of nAChRs in living human brain after smoking and smoking cessation. We performed [123]I-5IA SPECT on nonsmokers and smokers who had quit smoking for 4 h, 10 d, and

21 d and compared the distribution volumes (Vt) of ^{123}I-5IA of each group and with nonsmokers. To our knowledge, this is the first in vivo imaging study of nAChR upregulation and recovery in response to short-term smoking cessation in living subjects.

MATERIALS AND METHODS

Volunteers

Six male nonsmokers (23 ± 6 y) and 10 healthy male smokers (28 ± 4 y) were included in this study. Five smokers in the 4-h group were also included in either the 10-d or the 21-d group. In total, 21 ^{123}I-5IA SPECT studies were acquired (Table 1). None of the subjects had a history of neurologic or psychiatric illness or the use of psychotropic or sleep-inducing drugs. The nonsmokers had no history of smoking tobacco.

For the smoking withdrawal studies, the smokers were divided in 3 groups: 5 subjects (age, 28 ± 4 y) for 4-h withdrawal, 5 subjects (age, 27 ± 6 y) for 10-d withdrawal, and 5 subjects (age, 28 ± 3 y) for 21 d of smoking withdrawal. The 4 groups were age-matched.

All subjects gave written informed consent to participate in this study in compliance with the regulations of the Joint Committee on Clinical Investigation of the Kyoto University Hospital.

Radiolabeling

Radiolabeling of the ^{123}I-5IA followed the methods we reported previously (19). To a sodium ^{123}I-iodide solution (1,110 MBq) (Nihon Medi-Physics), 100 μg of (S)-5-(tri-n-butylstannyl)-3-((1-t-butoxycarbonyl-2(S)-azetidinyl]methoxy)pyridine, 1.5% acetic acid, 3 mol/L HCl, and 5% H_2O_2 solution were added, and the mixture was stirred at 75°C for 15 min. Concentrated HCl was then added, and the resulting solution was stirred for another 10 min at 75°C. The mixture was made basic with NaOH and extracted with ethyl acetate, and the organic layer was evaporated. The residue was purified by reverse-phase high-performance liquid chromatography ([HPLC] Cosmosil 5C18-AR-300, 10 × 250 mm; Nacalai Tesque; 10 mmol/L ammonium acetate/methanol/triethylamine = 752:750:2; 1.5 mL/min; retention time for 5IA was 40 min). After evaporation of the HPLC eluent, the residue was dissolved in 0.9% saline and filtered through a 0.2-μm filter into a sterile vial. Radiochemical purity was >98%, and radiochemical yields were ~42%. The specific activity determined from the ultraviolet absorbance at 254 nm was >169 GBq/μmol (the detection limit for this method).

SPECT

All subjects underwent a set of 5 SPECT dynamic scans (a 120-min scan, followed by 4 sets of 20-min scans). All SPECT dynamic scans were acquired with a triple-head rotating γ-camera system

TABLE 1
Study Groups

Nonsmokers	Smokers: period of smoking cessation		
	4 h	10 d	21 d
Subject 1	Subject 7	Subject 7	Subject 9
Subject 2	Subject 8	Subject 8	Subject 10
Subject 3	Subject 9	Subject 12	Subject 11
Subject 4	Subject 10	Subject 13	Subject 15
Subject 5	Subject 11	Subject 14	Subject 16
Subject 6			

(PRISM 3000; Picker International) equipped with low-energy, high-resolution, fanbeam collimators. Data acquisition and image reconstruction were performed as in our previous study (19). The data acquisition was alternately performed over 120 min after intravenous injection of ^{123}I-5IA, followed by 4 sets of 20-min scans (at 3, 4, 5, and 6 h after the injection). SPECT images were reconstructed using a filtered backprojection algorithm with a ramp filter. Attenuation correction was performed using ellipses outer line approximation and Chang's method (coefficient of 0.06/cm), which assumes that the attenuation process is homogeneous throughout the brain and can be described by an exponential function. Scatter correction was not applied.

A dose of ~150 MBq of ^{123}I-5IA was administered intravenously over a period of 1 min at a constant rate with an infusion pump, and the SPECT scan was started at the same time as the injection. Arterial blood sampling and metabolite correction were also performed to estimate the arterial input function of the ^{123}I-5IA for each volunteer by the same method as that used in our earlier study (19).

Arterial Input Function

Twenty-five arterial blood samples were obtained at the same time points as described previously (19). From each sample, 100 μL of plasma were removed and the radioactivity was measured in an automatic well-type γ-counter (Cobra 2; Packard Instruments). Sixteen samples were analyzed by thin-layer chromatography (TLC) (10% ammonium acetate and methanol [1:1], LK6DF Silica Gel, 60 Å; Whatman) for metabolite determination ($R_f = 0.55$ for ^{123}I-5IA) (19). The measured unmetabolized fractions were fitted with a dual exponential curve, and the input function was calculated as all plasma sample counts were corrected for metabolites using the fitted curve.

Data Analysis

Reconstructed SPECT images were automatically coregistered using a coregistration algorism of statistical parametric mapping, SPM99 (Welcome Department of Cognitive Neurology, London, U.K.), to minimize positional error caused by head movement during the scans. Multiple circular regions of interest (ROIs) (21 pixels per circle) were manually drawn in each brain region (basal ganglia, thalamus, brain stem, cerebellum, frontal, parietal, temporal, and occipital cortices) on both sides. ROI data were further decay-corrected. SPECT data were calibrated to the well counter used to measure the injected activity. Time–activity curves were generated from the ROIs and the dynamic image datasets.

Kinetic analysis of the ^{123}I-5IA was performed using a 2-compartment model including K_1 and k_2 rate constants and a curve-fitting method following our previous study (19). Vt values of the ^{123}I-5IA were calculated and used as a quantitative index correlated with the regional binding potential of the nAChRs. The Vt values were further evaluated in terms of interval change after the smoking withdrawal.

Statistical Analysis

All data are expressed as the mean ± SD. The Vt values obtained from the different regions in the brain were analyzed by 1-way ANOVA with the Bonferroni protected least significant difference test. The interval changes of the ^{123}I-5IA Vt were analyzed between the 3 phases after the smoking withdrawal using the Tukey–Kramer multiple comparison test. All tests were 2-sided, and probability values of $P < 0.05$ were considered significant.

– 242 –

RESULTS

As in our previous study (19), the characteristics of the arterial input functions for all volunteers (nonsmokers and smokers) were similar. The peak plasma activity occurred between 70 and 80 s after injection in all subjects and decreased rapidly to 6.5%–9.0% of the peak level in 10 min. Analysis of the unmetabolized compound by TLC demonstrated a high parent fraction of ^{123}I-5IA in the plasma (87.7% ± 6.3%) in the first minute. ^{123}I-5IA was rapidly metabolized, and the unchanged fraction represented 50.9% ± 8.8% and 32.4% ± 12.6% of total plasma activity at 20 and 60 min, respectively.

Figure 1 shows the representative standardized time–activity curve of ^{123}I-5IA in the frontal cortex. The concentrations of radioactivity were slightly higher in the nonsmokers and in the 4-h smoking-cessation group followed by the 10-d and 21-d smoking-cessation groups. The peaks of radioactivity occurred ~50 min after injection of ^{123}I-5IA for nonsmokers and for the 4-h and 21-d smoking-cessation groups, whereas it was at ~70 min for the 10-d smoking-cessation group. A differential dissociation of ^{123}I-5IA from the binding sites was noted in the brain. The 4-h smoking-cessation group showed a faster dissociation compared with that of the nonsmokers. However, the 10-d and 21-d smoking-cessation groups showed a slower dissociation than that of the nonsmokers (more pronounced in the 21-d group). These findings reflected a temporal change of the nAChRs in the human brain.

Packs per day and pack years of cigarette smoking before cessation were similar for the different groups of smokers (Table 2). Only 2 subjects (subjects 7 and 11) had detectable amounts of nicotine in their plasma after 4-h smoking cessation (Table 2).

To validate the V_t values of the nonsmokers as a baseline group, we compared (t test) our current data (nonsmokers) with our published data (19). No significant difference was observed between these groups. Similar findings were also seen for K_1 and k_2. Therefore, we used the V_t values from nonsmokers as a reference for further comparisons with groups of smokers at several smoking-cessation intervals.
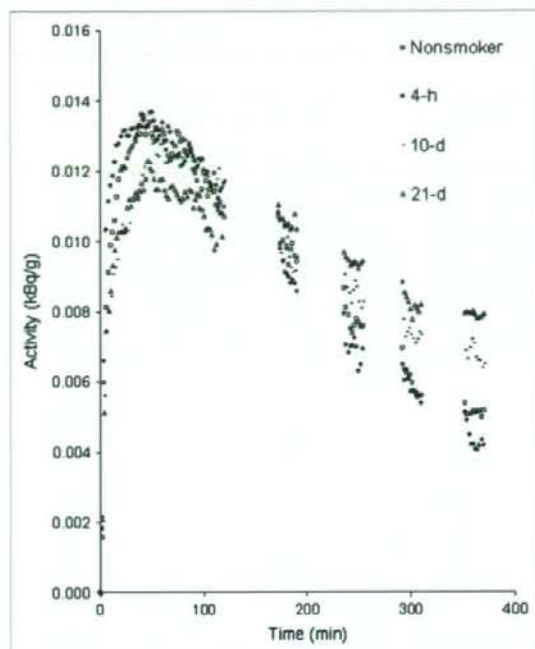

FIGURE 1. Representative standardized time–activity curves of ^{123}I-5IA in frontal cortex from a nonsmoker and smokers.

Table 3 describes the V_t values of different groups of volunteers (nonsmokers and smokers). There was a significant difference among those groups (ANOVA; $P < 0.001$). Individualized comparisons between 2 groups of volunteers were also performed. After 4 h of smoking cessation, the V_t values in all brain regions decreased significantly compared with those of the nonsmoker group ($P < 0.05$, except for frontal, parietal, and occipital cortices). On the other hand, after 10 d of smoking cessation, the V_t values were significantly higher than those of nonsmokers ($P < 0.05$, except for basal ganglia and thalamus). Then, after 21 d of smoking cessation, the V_t values decreased significantly compared

TABLE 2
Characteristics of Volunteers and Plasma Concentration of Nicotine and Cotinine

Group	Age (y ± SD)	Packs/d	Pack years	Plasma concentration (ng/mL)	
				Nicotine	Cotinine
Nonsmokers	24 ± 6	—	—	ND	ND
Smokers					
4-h withdrawal	28 ± 4	0.8 ± 0.3	6.1 ± 4.3	7.6, 8.9*	282 ± 189
10-d withdrawal	27 ± 6	0.8 ± 0.2	6.3 ± 3.9	ND	ND
21-d withdrawal	28 ± 3	0.8 ± 0.3	6.3 ± 4.5	ND	ND

*Results from only 2 subjects (3 other subjects had nondetectable values).

Packs/d = number of packs smoked per day; Pack years = number of packs per day while smoking multiplied by number of years smoked; ND = not detected (detection limits for nicotine and cotinine were 5.0 and 100 ng/mL, respectively).

Values are expressed in mean ± SD.

TABLE 3

^{123}I-5IA V_t Estimates for 2-Compartment, 2-Parameter Model for Various Brain Regions from Nonsmokers and Smokers
After Withdrawal of Cigarette Smoking

Subject	Frontal	Parietal	Temporal	Occipital	BG	Thalamus	BS	Cerebellum
Nonsmokers								
1	14.3	13.2	13.2	11.2	15.8	30.1	22.9	15.6
2	20.3	18.9	19.7	16.2	24.2	43.2	35.5	20.5
3	14.1	13.0	13.8	11.2	16.0	28.4	22.3	14.9
4	14.4	14.4	14.6	11.7	17.2	31.1	25.3	18.4
5	11.3	10.7	10.7	9.5	12.9	19.3	17.7	14.4
6	13.2	12.2	12.2	11.1	13.5	20.9	18.7	13.7
Mean	14.6	13.7	14.0	11.8	16.6	28.8	23.7	16.3
SD	3.0	2.8	3.1	2.3	4.0	8.6	6.4	2.7
Smokers								
4-h withdrawal								
7	6.1	6.3	6.4	5.9	6.5	7.0	7.0	5.9
8	12.6	13.0	12.2	11.4	12.8	16.1	14.0	11.3
9	14.9	14.0	13.7	12.5	15.0	21.3	19.4	14.4
10	8.7	8.4	8.6	7.6	10.0	13.5	12.2	8.8
11	10.2	10.4	10.2	9.0	11.2	12.9	12.3	10.0
Mean	10.5	10.4	10.2	9.3	11.1	14.1	13.0	10.1
SD	3.4	3.2	2.9	2.7	3.2	5.2	4.4	3.1
10-d withdrawal								
7	19.7	19.3	19.2	17.5	21.0	31.1	29.4	20.9
8	19.1	18.7	17.4	16.4	19.4	28.7	25.3	20.7
12	18.0	17.6	17.4	16.1	20.2	28.9	30.3	22.4
13	16.1	16.2	16.4	15.2	18.7	28.9	29.3	20.8
14	19.2	18.1	17.8	15.8	21.5	36.5	32.8	23.9
Mean	18.4	18.0	17.6	16.2	20.2	30.8	29.4	21.7
SD	1.4	1.2	1.0	0.9	1.2	3.3	2.7	1.4
21-d withdrawal								
9	15.3	14.6	14.6	12.2	17.6	28.4	23.6	19.7
10	14.4	14.3	13.8	12.1	17.5	31.3	24.9	17.2
11	17.0	16.6	15.9	13.6	18.5	27.0	26.1	20.1
14	14.1	14.0	13.6	12.8	15.5	21.6	21.0	15.7
15	14.4	14.1	13.6	12.2	15.7	27.0	22.7	15.7
Mean	15.1	14.7	14.3	12.6	17.0	27.0	23.7	17.7
SD	1.2	1.1	1.0	0.6	1.3	3.5	2.0	2.1

BG = basal ganglia; BS = brain stem.
Reported as mean for V_t estimates from 2-compartment model. Values for V_t are in mL/g.

with those of the 10-d group ($P < 0.01$, except for thalamus), returning to the level in nonsmokers (Vt values did not show any significant difference compared with those in the nonsmokers). Figure 2 shows the percentage of reduction and increment in each group of smokers in comparison with the nonsmoker group. In the Tukey–Kramer multiple comparison test, the interval changes of the ^{123}I-5IA Vt between the 3 phases after the smoking cessation were significantly different ($P < 0.001$).

The rate constant K_1 had some fluctuations among the different groups of volunteers (nonsmokers and smokers); however, these differences were not statistically significant (ANOVA; not significant) (Fig. 3A). On the other hand, the values of the rate constant k_2 were significantly different among the groups of volunteers (ANOVA; $P < 0.01$) (Fig. 3B). This difference was due basically to the increase of k_2 in the group with 4 h of smoking cessation.

DISCUSSION

The present study described the effect of nicotine intake in tobacco smokers and smoking cessation on the high-affinity nicotinic receptors in humans using ^{123}I-5IA SPECT. To our knowledge, this is the first in vivo imaging of nAChR upregulation and recovery in response to short-term smoking cessation in living smokers.

Previous animal studies have shown that chronic nicotine treatment induces an increase in high-affinity nicotinic receptor binding (6–9), and human postmortem studies have found a similar increase in ^{3}H-nicotine binding to high-affinity receptors in the postmortem cortex, cerebellum, and hippocampus of smokers compared with that in nonsmokers (10–12).

The mechanism by which the chronic exposure of nicotine evokes an increase in the density of the binding sites is not fully understood. Marks et al. reported that the increase in nicotinic receptor numbers in rodents is not caused by an
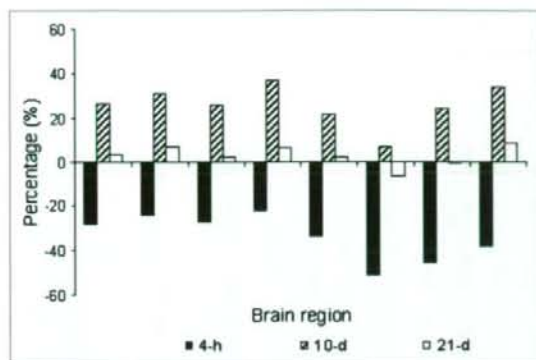
FIGURE 2. Percentage of reduction and increment of Vt of ^{123}I-5IA in smokers after smoking cessation compared with nonsmokers. Eight brain regions are frontal, parietal, temporal, occipital, basal ganglia, thalamus, brain stem, and cerebellum from the left, respectively.

increase in messenger RNA levels (20). The lack of an effect on nicotinic receptor transcription in mice suggests that nicotine-induced increases in nicotinic receptor levels are most likely related to a decrease in receptor turnover (21). The increase in nicotinic receptor number and the decreased rate of receptor turnover may be related to nicotinic receptor channel desensitization, which appears to reflect the conformational state of the receptor channel (21,22). Once the nicotinic receptor channels are desensitized and rendered inactive, additional receptors would be recruited to maintain the nicotinic response of the neuron, which results in an overall increase in nicotine binding, possibly due to a conversion of low-affinity receptors to a conformation with a high affinity for agonists (23).

In this study, the ^{123}I-5IA Vt measured at 4 h after smoking cessation was significantly lower than that in nonsmokers. The mean value of the calculated Vt of the smokers was ~33.5% ± 10.5% lower than that of nonsmokers and was more pronounced in the thalamus (51%) and brain stem (45%). In this group of volunteers, the plasma nicotine level 4 h after smoking cessation was detectable in only 2 subjects and was below the detection limit in the other subjects. Nicotine is highly lipophilic and demonstrated high levels of nonspecific uptake in brain (24,25). Rowell and Li have reported that levels of nicotine in the brain were ~3-fold higher than those in the plasma (7), which explains the lack of plasma nicotine measurements in 3 subjects in this group of volunteers. Because of high levels of nonspecific uptake of nicotine in the brain, nicotine or its metabolites may accumulate in nonspecific compartments in the brain (i.e., white matter) and then diffuse slowly into areas with higher levels of nAChRs, maintaining high levels of occupancy of the nAChRs. In addition, Brody et al. have shown saturation of the nicotinic receptors in human brain for up to 4 h in smokers (26). Thus, we would expect some level of nicotine or metabolites in the brain that would compete with ^{123}I-5IA

and impair imaging of the upregulation of nAChRs. Also, we believe that some level of nicotine in the brain resulted in a high level of occupancy of the receptors, which reduced specific tracer uptake (27). Because of competitive binding between the radioligand and nicotine in the brain, imaging of upregulation of nAChRs in vivo requires sufficient time for nicotine clearance (>4-h smoking cessation).

After 10 d of smoking cessation, the Vt of ^{123}I-5IA was significantly higher than that in nonsmokers, with a 25.7% ± 9.2% increase among brain regions. The result of the increased Vt of the ^{123}I-5IA was in agreement with the upregulation of the nAChRs in the brains of smokers reported in postmortem human studies (10–12) and in animal studies (6–9). Staley et al. have described similar findings in human brain (13). The authors noted that after 6.8 ± 1.9 d of tobacco abstinence, the uptake of ^{123}I-5IA increased significantly throughout the cerebral cortex (26%~36%) in smokers (13). After 10 d of smoking cessation, nicotine and cotinine were not detected in the plasma. Thus, blood nicotine levels were negligible in the ^{123}I-5IA SPECT scans of smokers as well as nonsmokers.

After 21 d of smoking cessation, the Vt of ^{123}I-5IA was significantly lower compared with that after 10 d of smoking cessation and was not significantly different from that in the nonsmokers. Breese et al. showed that smokers who had quit at least 2 mo before death had nicotinic receptor binding levels similar to those in nonsmokers (14). In the present study, the interval of 21 d was thought to be the recovery time during which upregulated nAChRs return to the level of the nonsmoker. This suggests that nicotine-induced upregulation of receptor number is a temporary effect, similar to that found in rodents (28,29).

The upregulation of the nAChRs was similar in almost all brain regions, except the thalamus and basal ganglia, which showed a slightly different pattern. In thalamus and basal ganglia, after 10 d of smoking cessation the Vt was higher than that of the nonsmokers, as in the other regions, but was not significantly different. Staley et al. have shown similar findings (13). In addition, it has been reported in a study of mice that nicotine-induced increases in nicotinic receptor numbers do not increase to the same degree in all brain regions (30). Moreover, the nicotinic receptor is more abundant in the thalamus, with greater receptor heterogeneity, than in other brain regions (19). However, the characteristics of the acute response of neuronal nAChRs to nicotine depend on their subunit composition (31,32). Nicotinic receptor subtypes are affected differentially by chronic exposure to nicotine, both in cell models (33–35) and in vivo (35). Multiple factors are thought to be responsible for these differences.

This study should be interpreted in the context of several limitations. (a) The number of subjects evaluated was small, which reduced the statistical accuracy. (b) The study design used did not allow us to deal with a within-subject analysis of the whole group, as the variables were analyzed independently. (c) The smokers varied in their rate and depth of inhalation of smoke, and these interindividual
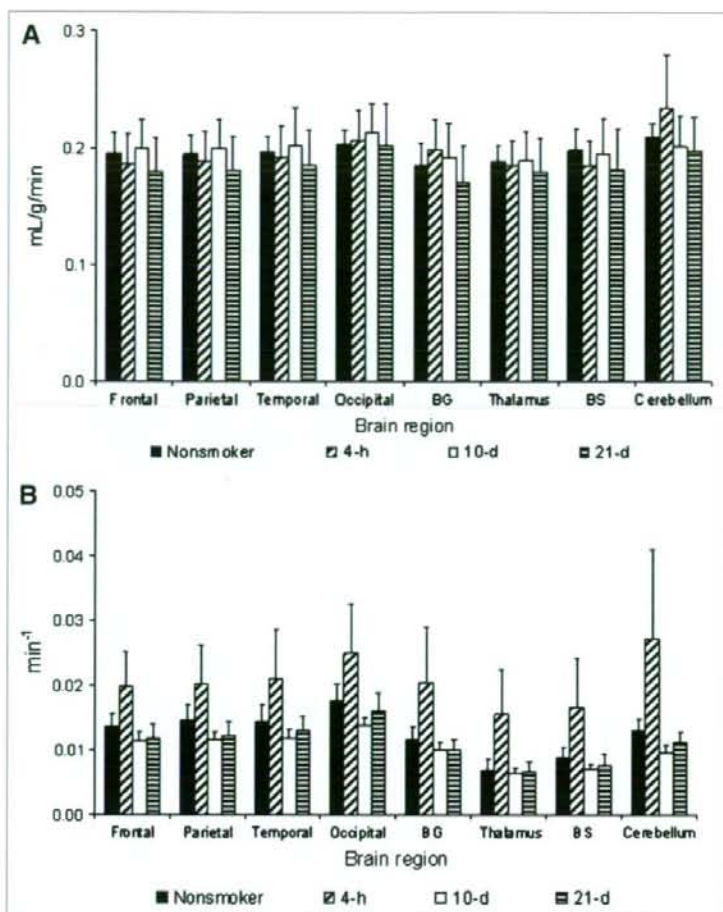
FIGURE 3. Temporal changes in rate constants K_1 and k_2 in nonsmokers and smokers after smoking cessation. (A) Rate constant K_1 (mL/g/min). (B) Rate constant k_2 (min^{-1}). BG = basal ganglia; BS = brain stem.

differences could have affected our measurements. (d) The detection limit of the plasma nicotine measurements was not enough to evaluate all blood samples. Thus, we were not able to correlate the plasma nicotine/cotinine levels with Vt. (e) We have not coregistered SPECT images with MRI, which would have been the most appropriate method for placement of ROIs. (f) We have not evaluated the smoker's behavior during the smoking-cessation period. We believe that the nicotine binding and desensitization of the nAChRs in the brain alleviate the cigarette craving and that craving will be the worst during the first 10 d of cessation due to the upregulation of nAChRs. The craving process should minimize after 21 d, as we observe similar levels of occupancy as nonsmokers at that time. However, we cannot exclude the possibility of other nAChR subtypes being involved in the process of tobacco dependence.

CONCLUSION

We have described the in vivo imaging of nAChR up-regulation and recovery in response to short-term smoking

cessation in smokers using [123]I-5IA SPECT. Our results clearly suggest that tobacco smoking is associated with an upregulation of nicotine binding sites in the brain. The up-regulation of the nAChRs of the smokers after chronic exposure to nicotine was downregulated to the level in non-smokers after ~21 d of smoking cessation. Thus, the upreg-ulation of receptor numbers is a temporary effect. Nicotine dependence and difficulty in smoking cessation are also interesting with regard to the findings of the [123]I-5IA SPECT study. The decrease in nicotinic receptors to nonsmoker levels may be the breaking point during the nicotine with-drawal period.

REFERENCES

1. Gotti C, Fornasari D, Clementi F. Human neuronal nicotinic receptors. *Prog Neurobiol.* 1997;53:199–237.

2. Paterson D, Nordberg A. Neuronal nicotinic receptors in the human brain. *Proc Neurobiol.* 2000;61:75–111.

3. Shimohama S, Kihara T. Nicotinic receptor-mediated protection against beta-amyloid neurotoxicity. *Biol Psychiatry.* 2001;49:233–239.

4. Decker MW, Rueter LE, Bitner RS. Nicotinic acetylcholine receptor agonists: a potential new class of analgesics. *Curr Top Med Chem.* 2004;4:369–384.

5. Buisson B, Bertrand D. Nicotine addiction: the possible role of functional up-regulation. *Trends Pharmacol Sci.* 2002;23:130–136.

6. Pietila K, Lahde T, Attila M, Ahtee L, Nordberg A. Regulation of nicotinic receptors in the brain of mice withdrawn from chronic oral nicotine treatment. *Naunyn Schmiedebergs Arch Pharmacol.* 1998;357:176–182.

7. Rowell PP, Li M. Dose-response relationship for nicotine-induced up-regulation of rat brain nicotinic receptors. *J Neurochem.* 1997;68:1982–1989.

8. Collins AC, Romm E, Wehner JM. Dissociation of the apparent relationship between nicotine tolerance and up-regulation of nicotinic receptors. *Brain Res Bull.* 1990;25:373–379.

9. Koylu E, Demirgoren S, London ED, Pogun S. Sex difference in up-regulation of nicotinic acetylcholine receptors in rat brain. *Life Sci.* 1997;61:L185–L190.

10. Perry DC, Davila-Garcia MI, Stockmeier CA, Kellar KJ. Increased nicotinic receptors in brains from smokers: membrane binding and autoradiography studies. *J Pharmacol Exp Ther.* 1999;289:1545–1552.

11. Teaktong T, Graham AJ, Johnson M, Court JA, Perry EK. Selective changes in nicotinic acetylcholine receptor subtypes related to tobacco smoking: an immunohistochemical study. *Neuropathol Appl Neurobiol.* 2004;30:243–254.

12. Kassiou M, Eberl S, Meikle SR, et al. In vivo imaging of nicotinic receptor upregulation following chronic (-)-nicotine treatment in baboon using SPECT. *Nucl Med Biol.* 2001;28:165–175.

13. Staley JK, Krishnan-Sarin S, Cosgrove KP, et al. Human tobacco smokers in early abstinence have higher of b2* nicotinic acetylcholine receptors than non-smokers. *J Neurosci.* 2006;26:8707–8714.

14. Breese CR, Marks MJ, Logel MJ, et al. Effect of smoking history on [³H]nicotine binding in human postmortem brain. *J Pharmacol Exp Ther.* 1997; 282:7–13.

15. Saji H, Ogawa M, Ueda M, et al. Evaluation of radioiodinated 5-iodo-3-(2(S)-azetidinylmethoxy)pyridine as a ligand for SPECT investigations of brain nicotinic acetylcholine receptors. *Ann Nucl Med.* 2002;16:189–200.

16. Musachio JL, Scheffel U, Finley PA, et al. 5-[I-125/123]Iodo-3(2(S)-azetidinylmethoxy)pyridine, a radioiodinated analog of A-85380 for in vivo studies of central nicotinic acetylcholine receptors. *Life Sci.* 1998;62:351–357.

17. Ueda M, Iida Y, Mukai T, et al. 5-[¹²³I]Iodo-A-85380: assessment of pharmacological safety, radiation dosimetry and SPECT imaging of brain nicotinic receptors in healthy human subjects. *Ann Nucl Med.* 2004;18: 337–344.

18. Vaupel DB, Tella SR, Huso DL, et al. Pharmacology, toxicology, and radiation dosimetry evaluation of [I-123]5-I-a-85380, a radioligand for in vivo imaging of cerebral neuronal nicotinic acetylcholine receptors in humans. *Drug Dev Res.* 2003;58:149–168.

19. Mamede M, Ishizu K, Ueda M, et al. Quantification of human nicotinic acetylcholine receptors with ¹²³I-5IA SPECT. *J Nucl Med.* 2004;45:1458–1470.

20. Marks MJ, Pauly JR, Gross SD, et al. Nicotine binding and nicotinic receptor subunit RNA after chronic nicotine treatment. *J Neurosci.* 1992;12:2765–2784.

21. Peng X, Gerzanich V, Anand R, Whiting PJ, Lindstrom J. Nicotine-induced increase in neuronal nicotinic receptors results from a decrease in the rate of receptor turnover. *Mol Pharmacol.* 1994;46:523–530.

22. Marks MJ, Burch JB, Collins AC. Genetics of nicotine response in four inbred strains of mice. *J Pharmacol Exp Ther.* 1983;226:291–302.

23. Bencherif M, Fowler K, Lukas RJ, Lippiello PM. Mechanisms of up-regulation of neuronal nicotinic acetylcholine receptors in clonal cell lines and primary cultures of fetal rat brain. *J Pharmacol Exp Ther.* 1995;275:987–994.

24. Broussolle EP, Wong DF, Fanelli FJ, London ED. In vivo specific binding of [³H]l-nicotine in the mouse brain. *Life Sci.* 1989;44:1123–1132.

25. Muzic R, Berridge M, Friedland R, Zhu N, Nelson A. PET quantification of specific binding of carbon-11-nicotine in human brain. *J Nucl Med.* 1998;39: 2048–2054.

26. Brody AL, Mandelkern MA, London ED, et al. Cigarette smoking saturates brain α4β2 nicotinic acetylcholine receptors. *Arch Gen Psychiatry.* 2006;63: 907–915.

27. Ding Y-S, Volkow ND, Logan J, et al. Occupancy of brain nicotinic acetylcholine receptors by nicotine doses equivalent to those obtained when smoking a cigarette. *Synapse.* 2000;35:234–237.

28. Collins AC, Bhat RV, Pauly JR, Marks MJ. Modulation of nicotine receptors by chronic exposure to nicotinic agonists and antagonists. *Ciba Found Symp.* 1990; 152:68–82.

29. Marks MJ, Stitzel JA, Collins AC. Time course study of the effects of chronic nicotine infusion on drug response and brain receptors. *J Pharmacol Exp Ther.* 1985;235:619–628.

30. Collins AC, Marks MJ, Pauly JR. Differential effect of chronic nicotine treatment on nicotinic receptor numbers in various brain regions of mice. *J Subst Abuse.* 1989;1:273–286.

31. Luetje CW, Patrick J. Both α and β subunits contribute to the agonist sensitivity of neuronal acetylcholine receptors. *J Neurosci.* 1991;11:837–845.

32. Fenster CP, Rains MF, Noerager B, Quick MW, Lester RAJ. Influence of subunit composition on desensitization of neuronal acetylcholine receptors at low concentrations of nicotine. *J Neurosci.* 1997;17:5747–5759.

33. Hsu Y-N, Amin J, Weiss DS, Wecker L. Sustained nicotine exposure differentially affects α3β2 and α4β2 neuronal nicotinic receptors expressed in *Xenopus* oocytes. *J Neurochem.* 1996;66:667–675.

34. Olale F, Gerzanich V, Kurytov A, Wang F, Lindstrom J. Chronic nicotine exposure differentially affects the function of human α3, α4 and α7 neuronal nicotinic receptor subtypes. *J Pharmacol Exp Ther.* 1997;283:675–683.

35. Peng X, Gerzanich V, Anand R, Wang F, Lindstrom J. Chronic nicotine treatment up-regulates α3 and α7 acetylcholine receptor subtypes expressed by the human neuroblastoma cell line SH-SY5Y. *Mol Pharmacol.* 1997;51:776–784.

Cardioprotective Effects of Erythropoietin in Rats Subjected to Ischemia–Reperfusion Injury: Assessment of Infarct Size with ^{99m}Tc-Annexin V

Tomoki Doue[1,2], Katsuichi Ohtsuki[1,2], Kazuma Ogawa[3], Masashi Ueda[4], Akihiro Azuma[1], Hideo Saji[5], Harry W. Strauss[6], and Hiroaki Matsubara[1]

[1]Department of Cardiology and Nephrology, Kyoto Prefectural University of Medicine, Kyoto, Japan; [2]Department of Medicine, Meiji University of Integrative Medicine, Nantan, Japan; [3]Division of Tracer Kinetics, Advanced Science Research Center, Kanazawa University, Kanazawa, Japan; [4]Radioisotopes Research Laboratory, Kyoto University Hospital Faculty of Medicine, Kyoto University, Kyoto, Japan; [5]Department of Patho-Functional Bioanalysis, Graduate School of Pharmaceutical Sciences, Kyoto University, Kyoto, Japan; and [6]Division of Nuclear Medicine, Department of Radiology, Memorial Sloan-Kettering Hospital, New York, New York

Administration of erythropoietin (EPO) during or immediately after myocardial ischemia can reduce subsequent myocardial apoptosis, a key phenomenon in myocardial ischemia–reperfusion injury. In this study, we assessed the effect of EPO on ^{99m}Tc-annexin V myocardial uptake and whether the accumulation of ^{99m}Tc-annexin V can predict cardiac remodeling and functional deterioration. **Methods:** Eighteen rats with left coronary artery (LCA) occlusion were randomized to receive either an intravenous injection of EPO (EPO group) or saline (nontherapy [nT] group) immediately after release of the occlusion. After 20 min of LCA occlusion and 30 min of reperfusion, the rats were injected with ^{99m}Tc-annexin V. One hour after ^{99m}Tc-annexin V injection, the LCA was reoccluded and ^{201}Tl was injected intravenously, and the rats were sacrificed 1 min later. The heart was removed and sectioned, and dual-tracer autoradiography was performed to evaluate the distribution of the area at risk (defined on the thallium autoradiograph) and the area of apoptosis (defined on the annexin autoradiograph). Adjacent histologic specimens had deoxyuridine triphosphate nick-end labeling (TUNEL) staining to confirm the presence of apoptosis and were compared with autoradiography. Another 16 rats were randomized to EPO and nT groups and underwent echocardiography immediately after release of the LCA occlusion and at 2 and 4 wk after surgery. **Results:** The areas of ^{99m}Tc-annexin V accumulation in the EPO group were smaller than those in the nT group, though the ^{201}Tl defect areas of these 2 groups were comparable (area ratio, 0.318 ± 0.038 vs. 0.843 ± 0.051, $P < 0.001$, for annexin and 24.8 ± 2.1 vs. 25.9 ± 2.6 mm^2, $P =$ NS, for thallium). ^{99m}Tc-annexin V accumulation correlated with the density of TUNEL-positive cells ($r = 0.886$, $P < 0.001$). In the nT group, left ventricular end-diastolic dimension (Dd) increased from baseline at 2 wk by $34.7\% \pm 3.8\%$ and remained stable at $34.9\% \pm 5.0\%$ at 4 wk after coronary occlusion. In the EPO group, Dd increased by $8.5\% \pm 2.1\%$ ($P < 0.01$ vs. nT at 2 wk) and $13.2\% \pm 2.8\%$ ($P < 0.01$ vs. nT at 4 wk). In the nT group, the left ventricular percentage of fractional shortening decreased by $42.2\% \pm 3.4\%$ and $52.9\% \pm 3.4\%$ at 2 and 4 wk, respectively, whereas in the EPO group it decreased $9.0\% \pm 1.9\%$ at 2 wk ($P < 0.01$ vs. nT at 2 wk) and $11.1\% \pm 6.7\%$ at 4 wk ($P < 0.01$ vs. nT at 4 wk). **Conclusion:** This study demonstrated that a single treatment with EPO immediately after release of coronary ligation suppressed cardiac remodeling and functional deterioration. ^{99m}Tc-annexin V autoradiographs and TUNEL staining confirm that this change is due to a decrease in the extent of myocardial apoptosis in the ischemic/reperfused region.

Key Words: ^{99m}Tc-annexin V; erythropoietin; reperfusion; apoptosis

Restoration of oxygen to ischemic myocardium induces apoptosis in the ischemic myocytes (1–4). In severe, prolonged ischemia, apoptosis occurs before necrosis during the later stages of ischemic injury (5,6). Elimination or reduction of apoptosis would reduce the infarction and the likelihood of cardiac remodeling and of decreased left ventricular (LV) function in the infarction region and, overall, could improve prognosis.

Although erythropoietin (EPO) was developed as a hematopoietic growth factor, stimulating the production and release of red blood cells, EPO has recently been shown to protect ischemic neural and myocardial tissue (7–9). The hematologic and neuro/cardioprotective roles of EPO are caused by the interaction of EPO with 2 different receptors. The classic EPO receptor is responsible for the red blood cell response, whereas the interaction with the β common-receptor is responsible for the tissue protective effects (10). In a rat study, EPO administration dramatically reduced infarct size, resulting in improvement of long-term cardiac contractility (11). A single dose of EPO administered immediately after release of coronary artery ligation reduced LV remodeling

and dysfunction in animals undergoing experimental myocardial infarction, though the dose of EPO was far above that usually used to treat anemia (12). Additional studies explored various doses and intervals between ischemic injury and EPO administration to preserve cardiac function after ischemia–reperfusion injury (12–14). The antiapoptotic effect of EPO has been suggested as the mechanism for myocardial preservation.

Under normal circumstances, phosphatidylserine, a constituent of membrane phospholipids, is actively restricted to the inner leaflet of the plasma membrane by the action of 2 enzymes, translocase and floppase. Early in the course of apoptosis, these enzymes are inactivated. As translocase and floppase are inactivated, scramblase, an enzyme that equilibrates the membrane lipids on the inner and outer leaflet of the cell membrane, is activated. This combination of enzyme inactivation and activation results in the rapid appearance of phosphatidylserine on the outer leaflet of the cell membrane (15).

Annexin V, a physiologic protein with a molecular weight of about 36 kD, binds with nanomolar affinity to membrane-bound phosphatidylserine (16,17). Both in vitro and in vivo methods have been developed that use this characteristic of annexin V binding to identify cells in the early stages of apoptosis (18–20). For example, Peker et al. have used ^{99m}Tc-labeled annexin V to detect apoptosis as a result of ischemia–reperfusion injury in vivo (21). Other investigators have used radiolabeled annexin V to identify apoptosis in acute cardiac allograft rejection, subacute myocarditis, and acute doxorubicin cardiotoxicity (20–22).

This study was performed to determine the effect of a single intravenous dose of EPO on apoptotic activity and ventricular function in animals subjected to ischemia–reperfusion.

MATERIALS AND METHODS

Materials

Mutant annexin V (annexin V-117, a recombinant human annexin engineered to include a binding site for technetium, generously provided by John Tait, University of Washington) was produced by expression in *Escherichia coli* as previously described (23). This material preserves phosphatidylserine-binding activity equivalent to that of native annexin V. Labeling efficiency was consistently above 92%, providing a specific activity of approximately 7.4 MBq per microgram of protein using a previously described radiolabeling protocol (23). Under these conditions, annexin V labeling was stable for at least 4 h.

Recombinant human EPO was kindly provided by Chugai Pharmaceutical Co., Ltd.

Animal Model of Ischemia and Reperfusion Injury

Eighteen Male Wister rats (10 wk old; body weight, 305 ± 12.4 g) were anesthetized with intraperitoneally administered pentobarbital (20 mg/kg) and intubated, and anesthesia was maintained with inhalation of 2% isoflurane in 1.0 L of oxygen/min during volume-controlled ventilation. The heart was exposed through a left thoracotomy; a pledgeted 5–0 silk suture on a small, curved needle was passed through the myocardium beneath the proximal portion of the left coronary artery (LCA); and both ends of the suture were passed

through a small vinyl tube to make a snare. The suture material was pulled tightly against the vinyl tube and secured by a keeper on the tube to occlude the LCA. Animals were randomized to receive either a single intravenous injection of EPO (200 units/kg in 0.3 mL of saline) or an equivalent volume of saline immediately after release of LCA occlusion (EPO group and nontherapy [nT] group, respectively, $n = 9$ in each). Myocardial ischemia was confirmed by ST-segment elevation on electrocardiography, regional cyanosis of the myocardial surface, and decreased regional wall motion. After a 20-min occlusion of the LCA, reperfusion was obtained by removal of the keeper and release of the snare and was confirmed by the change from cyanotic to pink in the myocardial risk area. During reperfusion, the snare was left loose on the surface of the heart for reocclusion. Approximately 55.5 MBq of ^{99m}Tc-annexin V were injected via a tail vein at 30 min after reperfusion. One hour after ^{99m}Tc-annexin V injection, the snare occluder was again pulled tightly and 0.185 MBq of ^{201}Tl was injected via a tail vein to delineate the area at risk. One minute later, the rat was euthanized by a bolus injection of 4 mL of 0.5 M KCl. The heart was excised, rapidly rinsed in saline, embedded in methylcellulose, and frozen in iced n-hexane. Serial short-axis heart sections (20- and 8-μm short-axis sections adjacent to each other) were obtained using a cryostat for autoradiography and histologic analysis, respectively. This study was approved by the institutional Animal Care Committee at Kyoto Prefectural University of Medicine.

Dual-Tracer Autoradiography

Dual-tracer autoradiography of the LV short-axis slices was performed using a bio-imaging analyzer system (BAS5000; Fuji Film). The apoptotic area was determined from the ^{99m}Tc-annexin V uptake area, and the area at risk was determined from the ^{201}Tl defect area. The first autoradiographic exposure was performed for 30 min to visualize ^{99m}Tc-annexin V. Approximately 72 h later (12 half-lives of ^{99m}Tc), the second exposure of the same heart sections was performed for 36 h to delineate the area at risk, expressed as ^{201}Tl defect area.

Data Analysis of Autoradiography

The extent and the density of the 2 radionuclides were quantitatively analyzed using the bio-imaging analyzer system. After exposure, the bioimaging plate was placed in a reader to determine the photostimulated luminescence (PSL) in each pixel (25×25 μm). These data were recorded for each animal and each nuclide. The accumulation of ^{99m}Tc-annexin V was assessed in 4 midventricular short-axis frozen sections. The region of decreased thallium activity seen on the autoradiograph was outlined, and the region of interest was transferred to the ^{99m}Tc-annexin V autoradiograph to evaluate ^{99m}Tc-annexin V uptake. Four background ROIs were set adjacent to the left ventricle in each autoradiograph, and the mean PSL per unit area (1 mm^2) of the 4 background ROIs was defined as background tracer uptake. The uptake values of each ROI were calculated as the background-corrected PSL per unit area (1 mm^2). The area ratio and the density ratio were defined as the indicator to evaluate the extent and intensity, respectively, of ^{99m}Tc-annexin V uptake. The area ratio calculated by dividing ^{99m}Tc-annexin V uptake area by ^{201}Tl defect area indicates the extent of the apoptotic area in the area at risk. The density ratio of ^{99m}Tc-annexin V was calculated by dividing the uptake values of the ^{99m}Tc-annexin V uptake area by that of the normally perfused area. All parameters were expressed as an average value obtained from the analysis of 4 midventricular short-axis slices in each rat.

Histopathologic Examinations

Four sets of short-axis frozen sections adjacent to the slices for autoradiography were stained with terminal deoxynucleotidyl transferase-mediated deoxyuridine triphosphate nick-end labeling (TUNEL) using a commercially available kit (in situ cell death detection kit, fluorescein isothiocyanate labeling; Roche Applied Science) according to the manufacturer's protocol. As a positive control of TUNEL staining, we used rat intestine. Rhodamine-labeled α-sarcomeric actinin (DAKO) was simultaneously used for the detection of muscular structures. Digital photographs were taken under confocal microscopy at 200× magnification. TUNEL-positive cardiomyocytes were counted in 20 randomly chosen fields within the area at risk for each section. The mean density ratio of ^{99m}Tc-annexin V was compared with the mean number of TUNEL-positive myocytes in the corresponding area of each rat. Another 2 sets of short-axis frozen sections adjacent to the slices for autoradiography were stained with hematoxylin and eosin and examined histopathologically by light microscopy.

Echocardiography

Sixteen 10-wk-old Wistar rats (body weight, 308 ± 15.6 g) were anesthetized (sodium pentobarbital, 30 mg/kg intraperitoneally) for a baseline ventricular function measurement by echocardiography (Sonos 5500 equipped with a 15-MHz phased-array transducer; Philips Electronics N.V.). The anesthetized rats were subjected to 20 min of myocardial ischemia and 30 min of reperfusion. Half the animals received a single intravenous injection of EPO (200 units/kg in 0.3 mL of saline) immediately after LCA occlusion (EPO group). The other rats received an equivalent volume of saline at the same time point (nT group). Echocardiography was performed immediately after release of the LCA occlusion and repeated at 2 and 4 wk after surgery. A parasternal long-axis view was recorded, ensuring that the mitral and aortic valves and the apex were visualized. A short-axis view was recorded at the level of the mid papillary muscles. Both 2-dimensional and motion-mode views were recorded at the same level. LV end-diastolic dimension (Dd) and end-systolic dimension (Ds) were measured from motion mode in both short- and long-axis views. The LV percentage of fractional shortening (%FS) in the long-axis view was calculated as %FS = (Dd − Ds)/Dd × 100. All measurements were taken and averaged over 5 consecutive cardiac cycles by 1 observer who was unaware of the treatment with EPO. The reproducibility of measurements was assessed at baseline by 2 sets of measurements in 10 randomly selected rats. The repeated-measures variability did not exceed ±5%. Blood (0.5 mL) was collected from the jugular vein under pentobarbital anesthesia just before and after operation and at 4, 10, and 28 d after operation to determine the hematocrit level (measured in triplicate).

Statistical Analysis

Results were expressed as mean ± SD. Statistical analyses were performed using a Windows computer with StatView software (version 5.0; SAS Institute Inc.). Comparisons between the 2 groups were made using an unpaired t test. The time course of the changes was compared by repeated-measures ANOVA with the Scheffé post hoc test. The relationship of ^{99m}Tc-annexin V uptake in the area at risk was correlated with the number of TUNEL-positive cells by linear regression. A value of P less than 0.05 was considered statistically significant.

RESULTS

### Autoradiographic Detection of Early Apoptotic Cells

Representative images of dual autoradiography are shown in Figure 1. In the nT group, ^{99m}Tc-annexin V accumulated strongly at the central zone of the myocardial area at risk, predominantly in the mid layer of myocardium. Compared with the nT group, the accumulation of ^{99m}Tc-annexin V was reduced in the EPO group. The areas of ^{99m}Tc-annexin V accumulation were smaller in the EPO group than in the nT group. Quantitative analyses demonstrated that the area ratio and density ratio of the EPO group were significantly smaller than those of the nT group (area ratio, 0.318 ± 0.038 vs. 0.843 ± 0.051, $P < 0.001$; density ratio, 22.2 ± 4.2 vs. 108.3 ± 14.0, $P < 0.0001$) (Fig. 2). The ^{201}Tl transmural defect areas of these 2 groups did not significantly differ in size (24.8 ± 2.1 vs. 25.9 ± 2.6 mm², $P = 0.56$).

Comparison of Histologic Findings with ^{99m}Tc-Annexin V Autoradiography

Figure 3 showed the representative tissue sections of TUNEL staining in each group. The myocardium in both groups showed no inflammatory cells, no necrotic cells, and no myocardial degeneration on the light microscopic examination of the hematoxylin- and eosin-stained slices. TUNEL-positive cells were scattered at the mid layer of the myocardial area at risk in the nT group. In contrast, TUNEL-positive cells were localized to a small area in the EPO group. In both groups, the distribution of TUNEL-positive cells agreed closely with

^{99m}Tc-annexin V ^{201}Tl
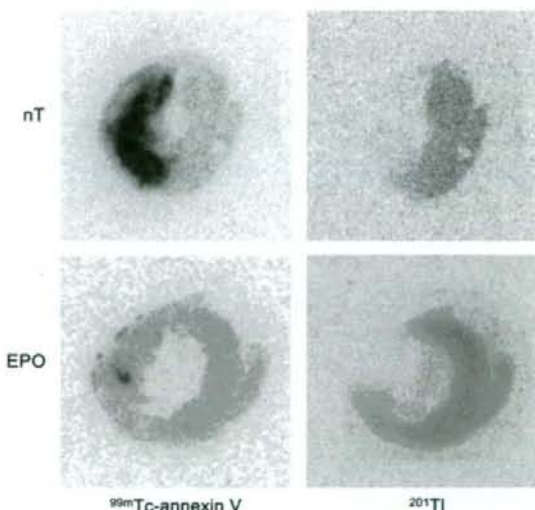
FIGURE 1. Autoradiography of ^{99m}Tc-annexin V and ^{201}Tl. Midventricular slices are shown from representative animals from each group. ^{99m}Tc-annexin V uptake area indicates myocardial apoptotic area, whereas ^{201}Tl defect area demonstrates area at risk. In nT group, ^{99m}Tc-annexin V highly accumulated at central zone of myocardial area at risk. Compared with nT group, accumulation of ^{99m}Tc-annexin V was reduced in EPO group with regard to both size and density.
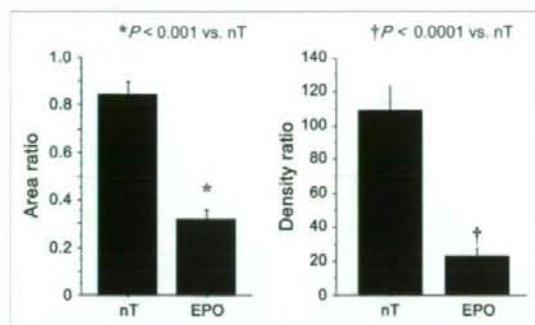
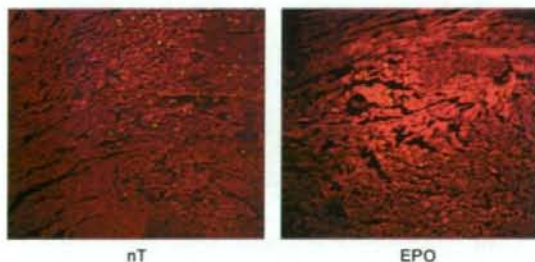FIGURE 2. Area ratio calculated by dividing ^{99m}Tc-annexin V uptake area by ^{201}Tl defect area would indicate extent of apoptotic area in area at risk. Density ratio calculated by dividing uptake value of ^{99m}Tc-annexin V uptake area by that of normally perfused area would reflect intensity of apoptosis in apoptotic area. Area ratio and density ratio of EPO group were significantly smaller than those of nT group (area ratio: 0.318 ± 0.038 vs. 0.843 ± 0.051, $P < 0.001$; density ratio: 22.2 ± 4.2 vs 108.3 ± 14.0, $P < 0.0001$).

FIGURE 4. Tissue sections of TUNEL staining were observed under confocal microscopy at 200× magnification. Density of TUNEL-positive cells (number of TUNEL-positive cells per HPF) in EPO group was significantly smaller than that of nT group (34.1 ± 11.7/HPF vs. 136.8 ± 25.9/HPF, $P < 0.01$).

^{99m}Tc-annexin V accumulation. Moreover, the density of the TUNEL-positive cells (the number of TUNEL-positive cells per high-power field [HPF]) in the EPO group was significantly smaller than that in the nT group (34.1 ± 11.7/HPF vs. 136.8 ± 25.9/HPF, $P < 0.01$) (Fig. 4).
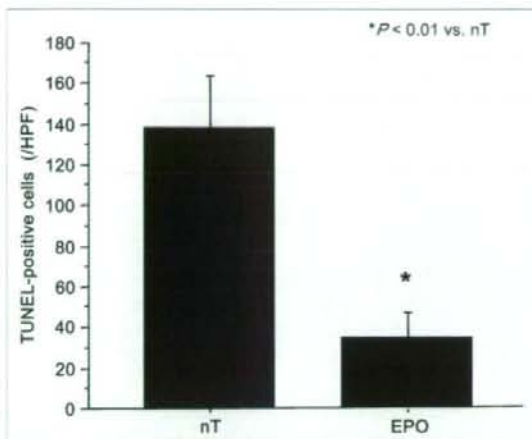
Figure 5 compares the density of TUNEL-positive cells in the representative myocardial apoptotic area (the number of TUNEL-positive cells per HPF) of each rat with the density of ^{99m}Tc-annexin V accumulation (PSL/m^2) in the corresponding area. The density of ^{99m}Tc-annexin V accumulation correlated well with the density of TUNEL-positive cells ($r = 0.886$, $P < 0.01$).

The Influence of EPO on Hematocrit

The average changes in hematocrit in rats treated with EPO (200 units/kg in 0.3 mL of saline) did not differ from those receiving an equivalent volume of saline just before and after operation and at 4, 10, and 28 d after operation (Table 1).

Echocardiography

Baseline (presurgery) measurements of LV cavity size (Dd) and LV systolic function (%FS) were similar in the groups assigned to EPO and nT. After coronary ligation/release, the depression in ejection fraction (36.1 ± 3.9 vs. 36.8 ± 3.1, $P = 0.91$) was similar in the 2 groups (Table 2).

Figure 6 illustrates the average changes in Dd and %FS at 2 and 4 wk after ischemia–reperfusion injury. In the nT group, Dd increased to a greater extent from 0 to 2 wk than from 2 to 4 wk. The percentage change in Dd at 2 and 4 wk after the surgical procedure, compared with baseline data immediately after ischemia–reperfusion injury, was 34.7% ±

FIGURE 3. Representative tissue section of TUNEL staining is shown in each group. TUNEL-positive cells were scattered at mid layer of myocardial area at risk in nT group. In contrast, TUNEL-positive cells were localized to very small area in EPO group.
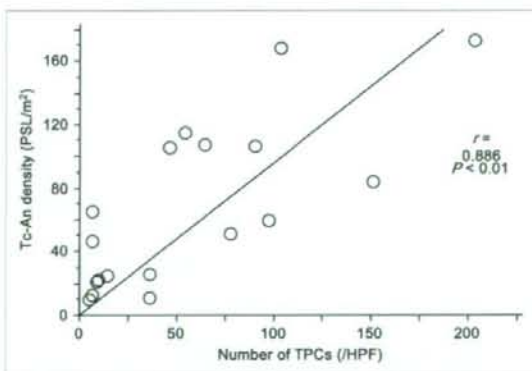

FIGURE 5. Comparison of density of TUNEL-positive cells in representative myocardial apoptotic area (number of TUNEL-positive cells per HPF) of each rat with density of ^{99m}Tc-annexin V accumulation (PSL/m^2) in corresponding area. Density of ^{99m}Tc-annexin V accumulation correlated well with density of TUNEL-positive cells ($r = 0.886$, $P < 0.01$).

Administered substance	Just before operation	Just after operation	Day 4	Day 10	Day 28
Saline (6)	40.9 ± 0.4	41.9 ± 0.4	42.6 ± 0.7	41.6 ± 0.4	40.9 ± 0.6
EPO (6)	40.1 ± 0.3	41.1 ± 0.4	42.3 ± 0.5	42.4 ± 0.5	42.6 ± 0.8

Data are mean percentage $\pm$ SD.

3.8% and 34.9% $\pm$ 5.0%, respectively. On the other hand, in the EPO group, the percentage change in Dd at 2 and 4 wk after ischemia–reperfusion injury was just 8.5% $\pm$ 2.1% ($P < 0.01$ vs. nT at 2 wk) and 13.2% $\pm$ 2.8% ($P < 0.01$ vs. nT at 4 wk), respectively.

A significant difference was observed in %FS between the EPO and nT groups over the 4-wk follow-up. Compared with the baseline data immediately after ischemia–reperfusion injury, %FS in the nT group declined by 42.2% $\pm$ 3.4% and 52.9% $\pm$ 3.4% at 2 and 4 wk. The LV performance of the nT group declined more steeply from 0 to 2 wk than from 2 to 4 wk. The %FS in the EPO group decreased slightly at 2 wk ($-9.0\% \pm 1.9\%$, $P < 0.01$, vs. nT at 2 wk) and 4 wk ($-11.1\% \pm 6.7\%$, $P < 0.01$, vs. nT at 4 wk).

These data suggest that the marked enlargement of the LV cavity and the steep decline of LV contractile function occurring in the nT group in the 2 wk after occlusion/release was suppressed by a single injection of EPO.

DISCUSSION

In this study, the extent of apoptosis after ischemia–reperfusion injury was markedly reduced after a single intravenous dose of EPO. This reduction of apoptosis was seen in histologic TUNEL staining of the myocardium in the area at risk and in autoradiographic studies with ^{99m}Tc-annexin V within 1 h of EPO administration. Moreover, echocardiography demonstrated that a single systemic administration of EPO immediately after coronary ligation minimized LV remodeling and preserved contractile function at 2 and 4 wk after surgery.

^{99m}Tc-annexin V has been reported to be highly sensitive in detecting apoptosis immediately after ischemia–reperfusion myocardial injury (24,25). ^{99m}Tc-annexin V has been used to

image injured myocardium after acute MI in patients undergoing acute coronary angioplasty (26). In 6 of 7 patients, increased uptake of ^{99m}Tc-annexin V was seen in the infarct area of the heart on early and late SPECT images, suggesting that apoptosis occurs in that area. Taki et al. reported similar findings with ^{99m}Tc-annexin V localization in the area at risk early after ischemia–reperfusion injury (14). The concentration of ^{99m}Tc-annexin V in the area at risk was concordant with the distribution of TUNEL-positive cells. In their study, ^{99m}Tc-annexin V accumulation was most prominent at 30–90 min after reperfusion and then gradually declined, whereas the number of TUNEL-positive cells peaked at 6 h to 1 d after reperfusion. In our study, ^{99m}Tc-annexin V accumulation clearly delineated the area of the apoptotic myocardium in the 20-min occlusion/30-min reperfusion model, consistent with the results of previous studies (14,24,25,). The previous investigation reported that, with TUNEL staining, EPO can limit the size of LV infarction (12). In this study, EPO therapy caused a 2.7-fold reduction of ^{99m}Tc-annexin V accumulation in the ischemic risk area.

Previous studies reported that a single administration of EPO increased the number of circulating reticulocytes by 3–4 d (reaching a maximum by days 8–11) (27,28). In the present study, the hematocrit in the rats treated with EPO did not differ from that in rats receiving saline just after operation and at 4, 10, and 28 d after operation. Therefore, the response

Index	Group	Before operation	After operation
LVDd (mm)	nT	6.2 ± 0.1	6.5 ± 0.2
	EPO	6.3 ± 0.1	6.6 ± 0.2
%FS	nT	61.3 ± 1.3	36.8 ± 3.1
	EPO	62.2 ± 0.9	36.1 ± 3.9

Data are mean $\pm$ SD.
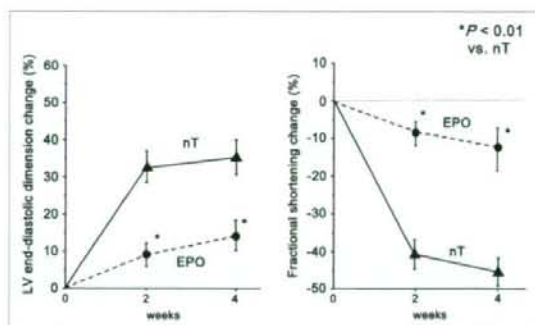
FIGURE 6. Changes in echocardiographic indices of LV size (Dd) and function (fractional shortening) during 4 wk after ischemia–reperfusion injury in EPO-treated and untreated rats. All indices are expressed as percentage change from baseline values (Table 2). *Significant difference ($P < 0.01$) between nT and EPO groups in percentage change in LV Dd and fractional shortening at weeks 2 and 4.

seen in the current experiment is unlikely related to an increase in the oxygen-carrying capacity of the blood.

The cardio- and neuroprotective properties are likely due to the interaction of EPO with the common β-receptor. This receptor requires a higher concentration of EPO and has the effect of reducing apoptosis. Previous studies in a rabbit model demonstrated that a single dose of EPO (5,000 units/kg) reduced infarct size from 35% to 13.8%, in keeping with the results in the present study (3). This acute effect persists over the subsequent 4-wk interval of observation. Previous observations have demonstrated a favorable influence of the antiapoptotic effect of EPO on long-term LV chamber size and function after myocardial ischemia (12,13). Moon et al. showed that a single dose of EPO at the onset of myocardial infarction reduced infarct size and reduced LV remodeling and dysfunction measured by echocardiography during the subsequent 8-wk period (12). Our results confirm that a single intravenous injection of EPO immediately after coronary occlusion suppressed LV remodeling and contractile deterioration at 4 wk after surgery. The results of ^{99m}Tc-annexin V autoradiography and TUNEL staining suggest that the beneficial effect of EPO is due to a remarkable suppression of apoptosis in the area at risk in this rat ischemia–reperfusion injury model. The mechanism of apoptosis reduction may be due to a phosphatidylinositol-3 kinase/Akt dependent pathway, as demonstrated in vivo in dog hearts (29).

Although prolonged administration of EPO is associated with adverse effects related to hematocrit elevation, such as hypertension and thromboembolic complications (30,31), a single administration of EPO, even at the higher doses used in this study, had a beneficial effect on the preservation of cardiac function after ischemia–reperfusion injury.

This study had 2 limitations. The first was the inability to assess the other effects of EPO on LV remodeling and function after myocardial infarction, though more recent studies reported that EPO possesses proangiogenic properties promoting neovascularization related to infarct size reduction after myocardial infarction (32). The second limitation was that we studied the feasibility of ^{99m}Tc-annexin V to assess the antiapoptotic treatment of EPO at only 1 time point, 30 min after the beginning of reperfusion. Further examination is needed to know the optimal timing for EPO injection as well as the optimum time for ^{99m}Tc-annexin V injection and imaging to assess the cardioprotective effect of EPO.

CONCLUSION

The present study demonstrated that ^{99m}Tc-annexin V is useful to evaluate myocardial apoptosis associated with ischemia–reperfusion injury. The ratio of the perfusion area at risk to annexin V lesion size is a useful indicator of myocardium salvaged by acute administration of EPO. The echocardiographic study showed that a single treatment with EPO immediately after coronary ligation suppressed cardiac remodeling and functional deterioration for at least 4 wk after the acute insult. These studies suggest that a single dose of EPO may be useful to prevent long-term cardiac remodeling and dysfunction after ischemia–reperfusion injury.

REFERENCES

1. Fliss H, Gautinger D. Apoptosis in ischemic and reperfused rat myocardium. *Circ Res.* 1996;79:949–956.
2. Gottlieb RA, Burleson KO, Kloner RA, et al. Reperfusion injury induces apoptosis in rabbit cardiomyocytes. *J Clin Invest.* 1994;94:1621–1628.
3. Parsa CJ, Matsumoto A, Kim J, et al. A novel protective effect of erythropoietin in the infarcted heart. *J Clin Invest.* 2003;112:999–1007.
4. Cai Z, Semenza GL. Phosphatidylinositol-3-kinase signaling is required for erythropoietin-mediated acute protection against myocardial ischemia/reperfusion injury. *Circulation.* 2004;109:2050–2053.
5. Maulik N, Kagan VE, Tyurin VA, et al. Redistribution of phosphatidylethanol-amine and phosphatidylserine precedes reperfusion-induced apoptosis. *Am J Physiol.* 1998;274:H242–H248.
6. Martin SJ, Reutelingsperger CP, McGahon AJ, et al. Early redistribution of plasma membrane phosphatidylserine is a general feature of apoptosis regardless of the initiating stimulus: inhibition by overexpression of Bcl-2 and Abl. *J Exp Med.* 1995;182:1545–1556.
7. Digicaylioglu M, Bichet S, Marti HH, et al. Localization of specific erythropoietin binding sites in defined areas of the mouse brain. *Proc Natl Acad Sci USA.* 1995;92:3717–3720.
8. Ehrenreich H, Hasselblatt M, Dembowski C, et al. Erythropoietin therapy for acute stroke is both safe and beneficial. *Mol Med.* 2002;8:495–505.
9. Sakanaka M, Wen TC, Matsuda S, et al. In vivo evidence that erythropoietin protects neurons from ischemic damage. *Proc Natl Acad Sci USA.* 1998;95:4635–4640.
10. Brines M, Grasso G, Fiordaliso F, et al. Erythropoietin mediates tissue protection through an erythropoietin and common beta-subunit heteroreceptor. *Proc Natl Acad Sci USA.* 2004;101:14907–14912.
11. Calvillo L, Latini R, Kajstura J, et al. Recombinant human erythropoietin protects the myocardium from ischemia-reperfusion injury and promotes beneficial remodeling. *Proc Natl Acad Sci USA.* 2003;100:4802–4806.
12. Moon C, Krawczyk M, Ahn D, et al. Erythropoietin reduces myocardial infarction and left ventricular functional decline after coronary artery ligation in rats. *Proc Natl Acad Sci USA.* 2003;100:11612–11617.
13. Parsa CJ, Jihee K, Riel RU, et al. Cardioprotective effect of erythropoietin in the reperfused ischemic heart. *J Biol Chem.* 2004;279:20655–20662.
14. Taki J, Higuchi T, Kawashima A, et al. Detection of cardiomyocyte death in a rat model of ischemia and reperfusion using ^{99m}Tc-annexin V. *J Nucl Med.* 2004;45:1536–1541.
15. Zwaal RFA, Schroit AJ. Pathophysiologic implications of membrane phospholipids asymmetry in blood cells. *Blood.* 1997;89:1121–1132.
16. Blankenberg FG, Katsikis PD, Tait JF, et al. In vivo detection and imaging of phosphatidylserine expression during programmed cell death. *Proc Natl Acad Sci USA.* 1998;95:6349–6354.
17. Blankenberg FG, Katsikis PD, Tait JF, et al. Imaging of apoptosis (programmed cell death) with ^{99m}Tc-labeled annexin V. *J Nucl Med.* 1999;40:184–191.
18. Fadok VA, Laszlo DJ, Noble PW, Weinstein L, Riches DW, Henson PM. Particle digestibility is required for induction of the phosphatidylserine recognition mechanism used by murine macrophages to phagocytose apoptotic cells. *J Immunol.* 1993;151:4274–4285.
19. Koopman G, Reutelingsperger CP, Kuijten GA, Keehnen RM, Pals ST, van Oers MH. Annexin V for flow cytometric detection of phosphatidylserine expression on B cells undergoing apoptosis. *Blood.* 1994;84:1415–1420.
20. Narula J, Acio ER, Narula N, et al. Annexin-V imaging for noninvasive detection of cardiac allograft rejection. *Nat Med.* 2001;7:1347–1352.
21. Peker C, Sarda-Mantel L, Loiseau P, et al. Imaging apoptosis with ^{99m}Tc-labeled annexin V in experimental subacute myocarditis. *J Nucl Med.* 2004;45:1081–1086.

22. Bennink RJ, van den Hoff MJ, van Hemert FJ, et al. Annexin V imaging of acute doxorubicin cardiotoxicity (apoptosis) in rats. *J Nucl Med.* 2004;45:842–848.

23. Tait JF, Brown DS, Gibson DF, et al. Development and characterization of annexin V mutants with endogenous chelation sites for ^{99m}Tc. *Bioconjug Chem.* 2000;11:918–925.

24. Dumont EA, Reutelingsperger CP, Smits JF, et al. Real-time imaging of apoptotic cell-membrane changes at the single-cell level in the beating murine heart. *Nat Med.* 2001;7:1352–1355.

25. Dumont EA, Hofstra L, van Heerde WL, et al. Cardiomyocyte death induced by myocardial ischemia and reperfusion: measurement with recombinant human annexin-V in a mouse model. *Circulation.* 2000;102:1564–1568.

26. Hofstra L, Liem IH, Dumont EA, et al. Visualisation of cell death in vivo in patients with acute myocardial infarction. *Lancet.* 2000;356:209–212.

27. Cheung WK, Goon BL, Guilfoile MC, et al. Pharmacokinetics and pharmaco-dynamics of recombinant human erythropoietin after single and multiple subcutaneous doses to healthy subjects. *Clin Pharmacol Ther.* 1998;64:412–423.

28. Eder H, Rosslenbroich B, Failing K. Erythropoietin reduces myocardial infarction and left ventricular functional decline after coronary artery ligation in rats. *Blut.* 1989;59:184–187.

29. Hirata A, Minamino T, Asanuma H, et al. Erythropoietin just before reperfusion reduces both lethal arrhythmias and infarct size via the phosphatidylinositol-3 kinase-dependent pathway in canine hearts. *Cardiovasc Drugs Ther.* 2005;19:33–40.

30. Roger SD, Baker LR, Raine AE. Autonomic dysfunction and the development of hypertension in patients treated with recombinant human erythropoietin (r-HuEPO). *Clin Nephrol.* 1993;39:103–110.

31. Wolf RF, Gilmore LS, Friese P, Downs T, Burstein SA, Dale GL. Erythropoietin potentiates thrombus development in a canine arteriovenous shunt model. *Thromb Haemost.* 1997;77:1020–1024.

32. van der Meer P, Lipsic E, Henning RH, et al. Erythropoietin induces neovascularization and improves cardiac function in rats with heart failure after myocardial infarction. *J Am Coll Cardiol.* 2005;46:125–133.

F-18 Fluorodeoxyglucose Uptake in a Solid Pseudopapillary Tumor of the Pancreas Mimicking Malignancy

Kotaro Shimada, MD,* Yuji Nakamoto, MD, PhD,* Hiroyoshi Isoda, MD, PhD,* Yoji Maetani, MD, PhD,*
Rikiya Yamashita, MD,* Shigeki Arizono, MD,* Yuusuke Hirokawa, MD,* Takashi Nitta, MD, PhD,†
Ryuichiro Doi, MD, PhD,† Hironori Haga, MD, PhD,‡ and Kaori Togashi, MD, PhD*

Abstract: Solid pseudopapillary tumors (SPTs), predominantly affecting young women, are rare pancreatic tumors. It is reported that imaging features of SPT are solid and cystic components, and there is intratumoral hemorrhage and calcification. However, findings of positron emission tomography (PET) using F-18 fluorodeoxyglucose (FDG) with pathologic correlation have not been fully evaluated. We present a case of SPT that mimicked malignancy on FDG-PET.

Key Words: solid pseudopapillary tumor, FDG, PET

(Clin Nucl Med 2008;33: 766–768)

S olid pseudopapillary tumor (SPT) was first described by Frantz in 1959 in a report of 3 cases and is currently classified as an epithelial neoplasm of uncertain cellular origin.[1] This is a unique tumor of low malignant potential most commonly affecting females of reproductive age, and a predilection for blacks and East Asians has been suggested.[2] It has been known that both positron emission tomography (PET) using F-18 fluoro-2-deoxy-D-glucose (FDG) and diffusion-weighted magnetic resonance imaging (DW-MRI) are useful for detecting abdominal tumors, but the number of reports describing FDG-PET and DW-MRI findings of SPT is still limited.[3–5] We report a rare case of SPT with imaging features on FDG-PET and DW-MRI and pathologic findings.

CASE REPORT

A 16-year-old female who had no remarkable past or family history underwent abdominal ultrasonography due to abdominal discomfort, and a mass was found in the pancreatic tail portion. The laboratory data, including tumor markers such as carcinoembryonic antigen (CEA), carbohydrate anti-

gen (CA) 19-9, CA125, Elastase-1, and duke pancreatic monoclonal antigen type 2, were all within normal ranges. A computed tomography (CT) scan with contrast enhancement revealed a round and slightly enhanced nodule approximately 1 cm in diameter in the pancreas tail, with no apparent calcification or necrosis (Fig. 1A). On magnetic resonance imaging (MRI), the nodule was depicted as a hypointense area on a T1-weighted image (T1WI) (Fig. 1B) and a slightly hyperintense area on a T2-weighted image (T2WI) with fat-suppression. The DW image demonstrated a homogenous abnormal signal intensity (Fig. 1C), and the apparent diffusion coefficient (ADC) value of the lesion was lower than normal pancreatic tissue on the ADC map. With regard to the PET findings, moderate to intense uptake of FDG was observed, corresponding to the lesion located in the pancreatic tail (Fig. 1D), with a maximum standardized uptake value (SUV) of 3.6. These findings suggested a solid pancreatic neoplasm that may have malignant potential in an adolescent girl. A nonfunctioning neuroendocrine tumor, pancreatoblastoma, and SPT were considered as differential diagnoses. The patient underwent distal pancreatectomy.

According to histopathological analysis, the tumor was solid and composed of sheets and nests of uniform polygonal epithelioid cells with round or oval nuclei and an acidophilic cytoplasm divided by thin fibrovascular stroma. Neoplastic cells supported by delicate vessels were intimately interdigitated into the non-neoplastic pancreas. Normal acinar tissues also remained within the tumor (Fig. 2A). Degenerative changes were seen in some parts of the tumor, and the remaining cells were arranged around delicate fibrovascular tissue containing small blood vessels in a pseudopapillary pattern (Fig. 2B). Cytoplasmic vacuolization and a cluster of foamy macrophages were also seen. Invasion of the vascular space or perineural invasion was not identified. The proliferation marker Ki-67 index was less than 1% and cellular atypia was mild. According to immunohistochemical analysis, the tumor cells were positive for CD56 and CD10 and negative for chromogranin A and AE1/AE3. These findings supported a final diagnosis of SPT of the pancreas.
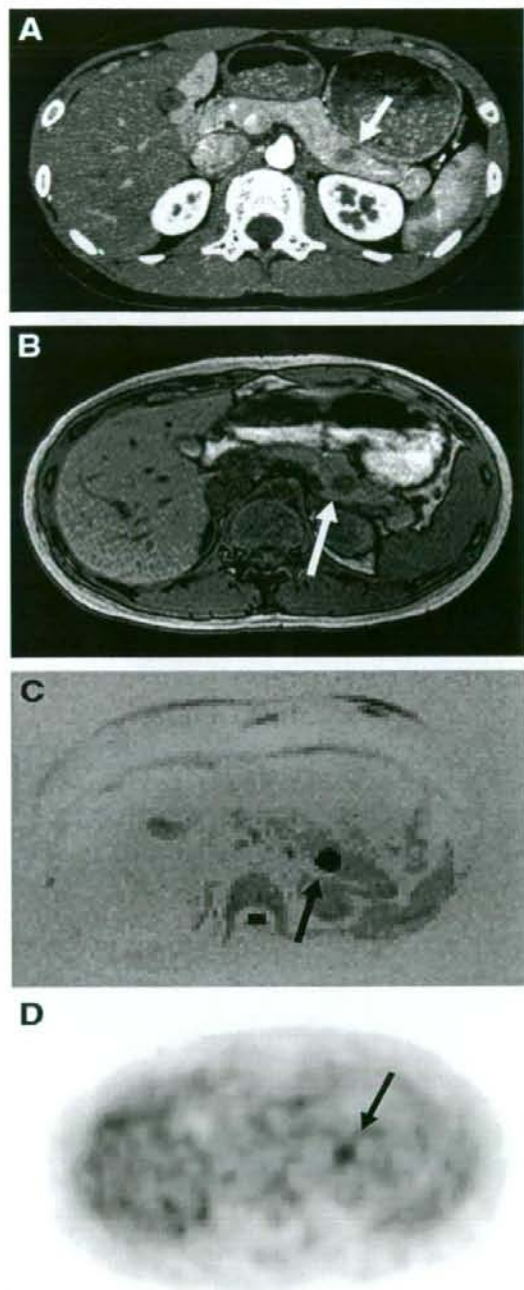
DISCUSSION

Solid pseudopapillary tumor of the pancreas is a rare type of pancreatic neoplasm found mainly in young woman; only approximately 9% of SPTs are found in men.[3] Surgery is

FIGURE 2. Low-power (A) and high-power (B) photomicrographs of hematoxylin and eosin stain are demonstrated. Low-power photomicrograph of this pathologic specimen shows that the tumor was solid with little degeneration such as hemorrhage and necrosis. High-power photomicrograph shows small eosinophilic cells with round or oval nuclei are arranged around fibrous connective tissue in a pseudopapillary pattern (B, arrow).

considered as a therapeutic method, and curative resection is usually possible for localized disease. Presenting symptoms are usually subtle and occasionally asymptomatic, so they are sometimes discovered at abdominal imaging, physical examination, or laparotomy performed for other reasons. Jaundice is rare, even in patients with lesions involving the head of the pancreas.

Based on pathologic features, SPT is slow-growing, is usually large, and is circumscribed or encapsulated by fibrous capsules, with marked degenerative and hemorrhagic change.[6,7] The tumors are usually round to ovoid and solitary

FIGURE 1. A contrast-enhanced CT shows a slightly enhanced nodule without calcification in the pancreas tail (A, arrow). Axial T1-weighted MR image shows a hypointense nodule with no evidence of hemorrhage in the pancreatic tail portion (B, arrow), and a diffusion-weighted image shows an abnormal signal intensity for this lesion (C, arrow). An axial PET image shows focal FDG accumulation in the left upper abdomen (D, arrow), corresponding to the pancreatic lesion, with a maximal SUV of 3.6.

767

and occur throughout the pancreas. Nearly all tumors have some component of cystic hemorrhagic or necrotic change regardless of size. Calcifications are occasionally seen most commonly in the capsule.[8,9] In our case, the tumor was small and solid, with little degeneration such as hemorrhage and calcification, which was not typical for SPT. However, it is also been reported that smaller tumors tend to be predominantly solid, whereas larger tumors tend to be more cystic because of degenerative changes with tumor growth.[10]

FDG-PET or PET/CT has been widely recognized as a useful imaging tool. FDG accumulation suggests a high glucose metabolic activity within the tissue, including not only neoplastic lesions but also various inflammatory foci, such as active pancreatitis or autoimmune pancreatitis.[11,12] In our case, relatively intense uptake of FDG was seen within the tumor, which is consistent with previous reports.[4,5] According to the histologic analysis, the Ki-67 index was less than 1% and cellular atypia was mild, suggesting that the malignant potential of this tumor was not high. In addition, no apparent inflammatory changes were seen around the lesion. Therefore, the positive finding of FDG-PET may be characterized by high cellular density with little degeneration, which is compatible with the abnormal signal on DW-MRI.

In conclusion, we report a case of SPT that was difficult to differentiate from malignancy because of focal uptake on FDG-PET and an abnormal signal on DW-MRI. This case demonstrated a pitfall of diagnostic imaging in that a small SPT with little degeneration can mimic malignancy on both FDG-PET and DW-MRI. We should keep in mind that SPT should not be excluded from differential diagnosis when it is clinically suspected, based on a patient's age or gender.

REFERENCES

1. Chung EM, Travis MD, Conran RM. Pancreatic tumors in children: radiologic-pathologic correlation. *Radiographics*. 2006;26:1211–1238.
2. Cantisani V, Mortele KJ, Levy A, et al. MR imaging features of solid pseudopapillary tumor of the pancreas in adult and pediatric patients. *AJR Am J Roentgenol*. 2003;181:395–401.
3. Shimizu T, Murata S, Mekata E, et al. Clinical potential of an antitumor drug sensitivity test and diffusion-weighted MRI in a patient with a recurrent solid pseudopapillary tumor of the pancreas. *J Gastroenterol*. 2007;42:918–922.
4. Lee JK, Tyan YS. Detection of a solid pseudopapillary tumor of the pancreas with F-18 FDG positron emission tomography. *Clin Nucl Med*. 2005;30:187–188.
5. Roldán-Valadez E, Rumoroso-García A, Vega-González I, et al. Non-resected solid papillary epithelial tumor of the pancreas: 18F-FDG PET/CT evaluation at 5 years after diagnosis. *Rev Esp Med Nucl*. 2007;26:160–164.
6. Procacci C, Graziani R, Bicego E, et al. Papillary cystic neoplasm of the pancreas: radiological findings. *Abdom Imaging*. 1995;20:554–558.
7. Rebhandl W, Felberbauer FX, Puig S, et al. Solid-pseudopapillary tumor of the pancreas (Frantz tumor) in children: report of four cases and review of the literature. *J Surg Oncol*. 2001;76:289–296.
8. Sclafani LM, Reuter VE, Coit DG, et al. The malignant nature of papillary and cystic neoplasm of the pancreas. *Cancer*. 1991;68:153–158.
9. Kosmahl M, Seada LS, Janig U, et al. Solid-pseudopapillary tumor of the pancreas: its origin revisited. *Virchows Arch*. 2000;436:473–480.
10. Mergo PJ, Helmberger TK, Buetow PC, et al. Pancreatic neoplasms: MR imaging and pathologic correlation. *Radiographics*. 1997;17:281–301.
11. Shreve PD. Focal fluorine-18 fluorodeoxyglucose accumulation in inflammatory pancreatic disease. *Eur J Nucl Med*. 1998;25:259–264.
12. Nakamoto Y, Saga T, Ishimori T, et al. FDG-PET of autoimmune-related pancreatitis: preliminary results. *Eur J Nucl Med*. 2000;27:1835–1838.